Popular Summary for

"High-Resolution Simulation of Hurricane Bonnie (1998). Part I: The Organization of Vertical Motion"

by

Scott A. Braun (NASA), Michael T. Montgomery (Colorado State University), and Zhaoxia Pu (Goddard Earth Science and Technology Center)

Submitted to the Journal of the Atmospheric Sciences

Hurricanes are well known for their strong winds and heavy rainfall, particularly in the intense rainband (eyewall) surrounding the calmer eye of the storm. In some hurricanes, the rainfall is distributed evenly around the eye so that it has a donut shape on radar images. In other cases, the rainfall is concentrated on one side of the eyewall and nearly absent on the other side and is said to be asymmetric. This study examines how the vertical air motions that produce the rainfall are distributed within the eyewall of an asymmetric hurricane and the factors that cause this pattern of rainfall. We use a sophisticated numerical forecast model to simulate Hurricane Bonnie, which occurred in late August of 1998 during a special NASA field experiment designed to study hurricanes. The simulation results suggest that vertical wind shear (a rapid change in wind speed or direction with height) caused the asymmetric rainfall and vertical air motion patterns by tilting the hurricane vortex and favoring upward air motions in the direction of tilt. Although the rainfall in the hurricane eyewall may surround more than half of the eye, the updrafts that produce the rainfall are concentrated in very small-scale, intense updraft cores that occupy only about 10% of the eyewall area. The model simulation suggests that the timing and location of individual updraft cores are controlled by intense, small-scale vortices (regions of rapidly swirling flow) in the eyewall and that the updrafts form when the vortices encounter low-level air moving into the eyewall.

High-Resolution Simulation of Hurricane Bonnie (1998). Part I: The Organization of Vertical Motion

Scott A. Braun*, Michael T. Montgomery%, and Zhaoxia Pu#

*Laboratory for Atmospheres, NASA/Goddard Space Flight Center, Greenbelt, MD

%Department of Atmospheric Sciences, Colorado State University, Fort Collins, CO

#Goddard Earth Science and Technology Center, NASA/Goddard Space Flight Center

Greenbelt, MD

submitted to

Journal of the Atmospheric Sciences

October 10

~~September 1~~, 2003

Corresponding Author: Dr. Scott A. Braun, Mesoscale Atmospheric Processes Branch, NASA/GSFC, Code 912, Greenbelt, MD 20771. Scott.A.Braun@nasa.gov.

Abstract

The Pennsylvania State University-National Center for Atmospheric Research mesoscale model MM5 is used to simulate Hurricane Bonnie at high resolution (2-km spacing) in order to examine how vertical wind shear impacts the distribution of vertical motion in the eyewall on the cloud scale. As in many previous studies, we find that the shear produces a wavenumber 1 asymmetry in the time-averaged vertical motion and rainfall. Several mechanisms for this asymmetry are evaluated. The simulation results show that the upward motion portion of the eyewall asymmetry is located in the downtilt direction, consistent with the vertical motion being that required to maintain dynamic balance. Variations in the direction and magnitude of the tilt are consistent with the presence of a vortex Rossby wave quasi-mode, which is characterized by a damped precession of the upper vortex relative to the lower vortex. The vertical motion asymmetry is also qualitatively consistent with an assumed balance between horizontal vorticity advection by the relative flow and stretching of vorticity, with relative asymmetric inflow (convergence) at low levels and outflow (divergence) at upper levels on the downshear side of the eyewall.

While the time-averaged vertical motion is characterized by weak ascent in a shear –induced wavenumber 1 asymmetry, the instantaneous vertical motion is typically associated with deep updraft towers that generally form on the southern side of the eyewall and dissipate on the northern side. The updrafts are frequently found on the trailing sides of eyewall mesovortices and result from an interplay between the wavenumber 1 forcing of vertical motion and the eyewall mesovortices, which rotate cyclonically around the eyewall. Specifically, the mesovortices contribute to upward motion by producing enhanced convergence on their trailing

sides where outflow associated with the mesovortex cyclonic circulation converges with low-level inflow associated with the large-scale shear.

1. Introduction

Early studies of the asymmetric structure of tropical cyclones found that the maximum precipitation tended to occur in the front quadrants relative to the storm motion. Several of these cases involved storms near coasts, so land influences may have played a role. Marks (1985) examined a case over the open ocean and also found a tendency for the maximum precipitation to occur in the front quadrants. This pattern of precipitation was suggested to be caused by the effects of boundary layer friction associated with a translating hurricane. Shapiro (1983), using a slab boundary layer model, showed that a translating storm develops asymmetries in the pattern of frictional convergence within the boundary layer such that the maximum convergence occurs immediately in front of the vortex.

More recent studies have demonstrated an important influence of environmental vertical wind shear on the asymmetric structure of hurricanes. Corbosiero and Molinari (2003) examined lightning data in tropical cyclones ranging from depressions to tropical storms to hurricanes. They found that lightning occurrence showed a marked downshear tendency that increased with the strength of the shear. In the inner core, storms in environments with shear less than 10 m s^{-1} exhibited little left-right preference relative to the shear vector, but for stronger shear, a clear left signal was present. For the outer bands, in moderate to strong shear (>5 m s^{-1}), there was a clear downshear right signal. These relationships held irregardless of storm intensity or of the underlying surface (land or ocean).

Several mechanisms have been proposed by which vertical shear produces asymmetries in vertical motions in adiabatic vortices. This shear can be associated with the environmental winds or with beta gyres caused by the advection of planetary vorticity by the hurricane vortex (Wang and Holland 1996a; Bender 1997). Bender (1997) has shown that the weakening of beta gyres

with height can produce vertical shear on the order of 5 m s^{-1} over the depth of the troposphere.

One mechanism for generating asymmetric vertical motion is related to the tilting of the vortex by the vertical shear (Raymond 1992; Jones 1995; Wang and Holland 1996a; Frank and Ritchie 1999). In order for the vortex to remain balanced, the isentropes must be raised in the direction of tilt and lowered on the other side, i.e., a negative potential temperature anomaly occurs downtilt and a positive anomaly uptilt. This effect is accomplished by upward (downward) motion on the downtilt (uptilt) side of the vortex. Jones (1995), Wang and Holland (1996a, 1996c), and Frank and Ritchie (1999) showed that this mechanism is only active for a brief period after tilting of the adiabatic vortex, after which time a second mechanism becomes important. Since the temperature anomaly is fixed with respect to the vortex tilt, the second mechanism for vertical motion occurs as the vortex flow moves adiabatically through the temperature anomalies (Jones 1995). Upward motion occurs as the air moves from the positive to the negative temperature anomalies and downward motion occurs as air moves from the negative to the positive anomalies. Consequently, the vertical motion is 90 degrees out of phase with the temperature anomalies with the upward motion to the right of the direction of vortex tilt. Note that the location of upward motion is described in relation to the tilt direction rather than the direction of shear. In many cases, the directions of tilt and shear may be different as a result of the mutual interaction and co-rotation of the upper- and lower-level vortices (Jones 1995; Reasor and Montgomery 2001; Reasor et al. 2003).

Wang and Holland (1996b, 1996c), Bender (1997) and Frank and Ritchie (1999, 2001) have shown that, whether the shear comes from the environmental flow or from the beta gyres, the upward motion part of the asymmetry in a diabatic vortex usually occurs downshear or slightly downshear-left while the precipitation is typically left of the shear. A proposed

mechanism for the downshear maximum in upward motion in diabatic vortices is related to the relative flow within the vortex (Willoughby et al. 1984; Bender 1997; Frank and Ritchie 2001). If the vortex moves with the ambient flow at a particular level, called the steering level, then there will be flow relative to the vortex above and below the steering level. The hurricane inner core is a region of high vorticity with strong vorticity gradients near the eyewall. Conservation of vorticity suggests that strong vorticity advection must be balanced by stretching or compression of vorticity. As a result, where the relative flow is directed inward, the negative vorticity advection is balanced by vortex stretching associated with convergence, and vice versa. For a vortex in linear shear, low-level inflow and upper-level outflow occur on the downshear side of the vortex, thereby producing low-level convergence and upper-level divergence and a deep layer of upward vertical motion. The opposite occurs on the upshear side of the vortex.

Diabatic vortices generally have much smaller tilts than their adiabatic counterparts, usually much less than the radius of maximum winds. It has been argued that the diabatic heating associated with convection opposes the tilting by more strongly coupling the lower and upper vortices (Wang and Li 1992; Flatau et al. 1994; Wang and Holland 1996c). Reasor et al. (2003) have argued that the moist dynamics associated with diabatic vortices are not fundamentally different than the adiabatic dynamics. First, they showed that, as long as the shear is not too strong, adiabatic vortices are quite resilient to shear. They examined the tilting of a vortex by shear and found that a damping mechanism intrinsic to the dry adiabatic dynamics suppresses departures from an upright state. This realignment occurs through projection of the tilt asymmetry onto two types of vortex Rossby waves: a quasi-mode, or discrete, vortex Rossby wave that causes long-lived precession of the upper part of a tilted vortex relative to the lower part, and sheared vortex Rossby waves in which the radial shear of the swirling flow

axisymmetrizes tilt asymmetries, resulting in short-lived precession and more rapid reduction of the tilt. They suggested that the effects of moisture simply enhance this process.

Black et al. (2002) described the structure of eastern Pacific hurricanes Jimena (1991) and Olivia (1994) using aircraft radar and flight-level in-situ data. Jimena was able to maintain category-4 intensity despite estimated vertical shear of 13-20 m s^{-1} while Olivia strengthened in 8 m s^{-1} shear. In both cases, shear produced a wavenumber-1 distribution of convection with the highest reflectivities in the semicircle to the left of the shear direction. The convective cells comprising this reflectivity asymmetry were periodic, with echoes forming on the downshear side of the eyewall, growing and maturing on the left side of the shear vector, and often dissipating on the upshear side. In some cases, clusters of cells were observed to move around the eyewall multiple times, initiating new bursts of convection as they moved again into the downshear portion of the eyewall. The clusters of cells typically moved more slowly than the mean flow near the radius of maximum wind, consistent with the presence of vortex Rossby waves (Montgomery and Kallenbach 1997; Chen and Yau 2001; Fulton 2001).

This study examines a high-resolution simulation of Hurricane Bonnie (1998) using the Pennsylvania State University-National Center for Atmospheric Research (PSU-NCAR) mesoscale model (MM5) for the purpose of demonstrating the impact of vertical shear on the distribution of vertical motion in the eyewall. Heymsfield et al. (2001) described the structure of Hurricane Bonnie on August 23, 1998, using multiple observations from the National Aeronautics and Space Administration (NASA) Convection And Moisture EXperiment (CAMEX-3). On that day, Bonnie's structure was highly asymmetric with strong low-level reflectivities on the eastern side of the storm and little precipitation on the western side. Observations from the NASA ER-2 Doppler radar indicated isolated deep convective towers on

the eastern side of the storm with updrafts greater than 10 m s^{-1}. Heymsfield et al. (2001) developed a conceptual model for the evolution of the convective towers in which the updrafts formed near the top of the boundary layer on the southern side of the eyewall and grew progressively taller while moving around to the northern side. In other words, the convection was viewed in terms of rising plumes of air that were initiated to the south and reached the upper troposphere to the north of the eye. Results from the numerical simulation will be used to examine the mechanisms by which vertical shear causes the asymmetric structure of vertical motion and precipitation. Furthermore, because of the small grid spacing (2 km), we go beyond previous studies and examine the processes controlling the timing and location of individual updrafts and relate these findings, and those of Black et al. (2002), to the vorticity dynamics of the eyewall. The results will also be compared to the conceptual model of Heymsfield et al. (2001) to determine the extent to which this conceptual model explains vertical motions and precipitation growth in the eyewall.

Section 2 provides an overview of Bonnie's synoptic environment, its precipitation structure as measured by the NASA Tropical Rainfall Measurement Mission (TRMM) satellite, and the relationship between the storm's structure and intensity changes to the evolution of the large-scale winds and vertical shear. Section 3 summarizes the numerical model configuration, physics options, and initial conditions, as well as provides some basic validation of the numerical simulation. Section 4 describes the time-averaged structure and explains the relationship between the simulated wavenumber 1 asymmetry in vertical motion and the vertical wind shear. Section 5 describes the time-varying structure of the eyewall vertical motions and examines the role that eyewall mesovortices play in determining the timing and location of updrafts. Finally, conclusions are provided in section 6.

2. Synoptic discussion

For the purpose of evaluating the large-scale environmental influences on hurricane Bonnie, particularly Bonnie's precipitation structure, a high-resolution version of the European Center for Medium-Range Weather Forecasts (ECMWF) analyses was obtained from NCAR. These analyses, available every six hours and with horizontal resolution of 1.125 degrees, were then interpolated to a grid with 1° resolution by the NASA Data Assimilation Office. Estimates of the environmental winds and wind shear over Hurricane Bonnie were obtained by averaging the wind information over a 5°-radius circle centered on the storm at each time. Figure 1 shows horizontal plots of geopotential height and winds at 850 and 200 hPa for 1200 UTC 22 and 1200 UTC 24 August, which generally encompasses the period of the MM5 simulation. Figure 2 shows the area-averaged zonal and meridional wind components as well as a time series of the 850-200 mb wind shear.

Bonnie formed as a tropical depression at 1200 UTC 19 August and slowly developed into a tropical storm by 1200 UTC 20 August and into a hurricane by 0000 UTC 22 August. During this development period, the storm was embedded in generally southeasterly flow (Figs. 1a, 1b) with moderate, but decreasing shear (Fig. 2). On 22 August, the shear diminished and the storm rapidly intensified. Radar reflectivity data from the TRMM precipitation radar during an overpass at 1800 UTC 22 August (Fig. 3a) showed a well-defined eyewall with heavy precipitation concentrated on the northern and southeastern portions of the eyewall and multiple convective rainbands and broad stratiform precipitation generally to the north and east of the center. While not symmetric in structure, precipitation surrounded much of the storm center.

Between 22 and 24 August, Bonnie approached a weak, nearly stationary upper-level trough over the southeastern United States (Figs. 1b, 1d). Upper-level flow switched from

southeasterly to northwesterly and the vertical wind shear increased significantly. Concomitantly, further intensification of Bonnie was halted (Fig. 2c). As suggested by the storm's track in Fig. 1 (see also Fig. 5), the northwesterly flow significantly retarded the northwesterly movement of Bonnie. By 24 August (Fig. 1c,d), westerly flow at 200 hPa associated with the trough clearly impinged on the western side of the storm. The increased shear led to a highly asymmetric precipitation structure (Fig. 3b) with precipitation concentrated primarily to the east of the center while the storm's intensity remained relatively constant. Upon relaxation of the shear and a return to southerly flow on 25 August (Fig. 2), Bonnie began to move more rapidly to the northwest. Bonnie subsequently underwent an eyewall replacement cycle (Zhu et al. 2003) prior to making landfall in North Carolina late on 26 August.

3. Simulation description and validation

a. Model description

The model used in this study is the PSU-NCAR non-hydrostatic fifth generation mesoscale model (MM5 V3.4; Dudhia 1993; Grell et al. 1995). Because of computational limitations, the simulation was conducted in two steps. First, a coarse-resolution simulation was performed using an outer mesh (Fig. 4) with 36-km horizontal grid spacing, 91×97 grid points in the x and y directions, respectively, and 27 vertical levels. A second inner mesh with 12-km horizontal grid spacing consisted of 160×160 grid points. The simulation was started at 1200 UTC 22 August 1998 and run for 36 hours, with model output saved every hour. Physics options for the coarse-grid simulation included a modified version of the Blackadar planetary boundary layer scheme in which surface roughness calculations for momentum, temperature, and moisture follow Garratt (1998) and Pagowski and Moore (2001). Cloud processes were represented by the Grell cumulus parameterization scheme and a modified version of the Goddard Cumulus Ensemble model cloud

microphysics (see the appendix). Shortwave radiative processes were represented by the cloud-radiation scheme of Dudhia (1989) while longwave radiation used the Rapid Radiative Transfer Model (RRTM) of Mlawer et al. (1997) and were calculated every five minutes. Although heating associated with the dissipation of turbulent kinetic energy near the surface has been shown to have an impact on hurricane intensity (Bister and Emanuel 1998; Zhang and Altshuler 1999), this effect has not been included in this study.

Initial and boundary conditions were obtained from 12-hourly global analyses from the ECMWF archived at NCAR. Analysis fields, including temperature, relative humidity, geopotential height, and winds at mandatory pressure levels and with horizontal resolution of 2.5° were interpolated horizontally to model grid points (the higher-resolution ECMWF analyses used in section 2 were obtained well after simulations were begun). These interpolated analyses were refined by adding information from standard twice-daily rawinsondes and three-hourly surface and buoy reports using a Barnes objective analysis technique (Manning and Haggenson 1992). Final analyses were then interpolated to the model vertical levels.

Because the large-scale analysis did not contain an adequate representation of the initial hurricane vortex, a bogusing technique using four-dimensional variational data assimilation developed by Zou and Xiao (2000) and Xiao et al. (2000) and modified by Pu and Braun (2001) was used. See Pu and Braun (2001) for a complete description of the methodology. The assimilation was performed on the 36-km grid only. A bogus sea-level pressure field was specified using the analytic profiles proposed by Holland (1980) while the tangential winds were derived by assuming gradient wind balance. Bogus winds above the surface were obtained by multiplying the surface wind values by an empirical function, as suggested in Kurihara et al. (1993), that decreased with height from a value of 1 in the boundary layer to zero above about

200 hPa. The initial central sea-level pressure, maximum wind speed, and radius of maximum wind were prescribed as 970 hPa, 45 m s^{-1}, and 120 km, respectively. Pu and Braun (2001) found that use of a larger than observed radius of maximum wind produced better results because the 36-km grid was incapable of resolving the structure of the eye when the observed radius (about 40 km in this case) was used.

A high-resolution simulation was conducted by using 1-h output from the 36- and 12-km grids to provide initial and boundary conditions for a 6-km grid (225×225×27 grid points) and 2-km grid (226×226×27) starting at 6 h into the forecast to allow for some model spin up on the 12-km grid. The high-resolution grids were run for 30 hours until 0000 UTC 24 August. The 2-km grid was moved hourly to keep it centered on the storm. Model physics were identical to the coarse-grid simulation except that no cumulus parameterization scheme was used and model output was saved every 15 minutes. The high-resolution simulation was repeated for the period between 24-30 h with model output every 3 min in order to resolve the evolution of individual updrafts.

For most applications, including computation of storm motion and compositing of output fields to a storm-relative grid, the storm center was determined, as in Braun (2002), at every model output time using the pressure field at the lowest model level. The horizontal distribution of pressure was used to determine an approximate geometric center, or centroid, of the pressure field. The location of the minimum pressure was used as a first guess for the center. A variational approach was then used that adjusts the location of the center until the azimuthal variance of the pressure field at all radii between the center and the outer portion of the eyewall (~ 65 km) was minimized. This methodology worked well not only for identifying the centroid of the pressure field but also the approximate centroid of the ring of strong tangential winds and vorticity. Storm

motion was then computed from the identified center locations. To compute the time-averaged fields in section 4, model output fields were transferred to a grid in which the storm's center was fixed with respect to both height and time.

The environmental winds in the region of the storm were estimated by averaging the horizontal wind components over a circular region within 300 km of the storm center using output from the 6-km grid. Because of the relatively small averaging area, the effects of beta gyres are included within this estimate of the environmental winds. This means that the environmental shear described in later sections is a combination of the environmental flow and the effects of the beta gyres weakening with height.

b. Simulation validation

In this section, we provide a basic validation of the simulated track, intensity, and precipitation structure. Figure 5 compares the simulated track to that observed. Because of the use of the bogus vortex, the initial error is very small and is approximately equal to the grid spacing of the second nest (12 km). During the first 12 to 18 h, the simulated storm exhibits an eastward drift and, in the following 18 h, the storm exhibits a northwesterly drift relative to the observations. As discussed in more detail below, the more rapid movement of the simulated storm to the northwest may result from an underestimation of the northwesterly flow aloft within the model.

The simulated intensity is depicted in Fig. 6 in terms of both the minimum sea-level pressure and the maximum surface wind speed. Data from the first 6 hours is obtained from the 12-km grid while information at later times is from the 2-km grid. The simulated minimum sea-level pressure compares quite favorably with that observed since it is generally within 5-10 hPa of the observed value. During the first 24 h of simulation, the trend in the minimum sea-level

pressure also agrees quite well with observations while in the last 12 h the simulated storm shows a greater deepening rate than observed.

Two estimates of the maximum simulated surface winds are shown in Fig. 6b. The thin solid line shows the maximum wind at the lowest model level while the dashed line shows the maximum azimuthally averaged wind speed at the same level. These results are compared to the estimated maximum surface winds measured within Bonnie by reconnaissance aircraft. The simulated maximum surface winds show significant intensification during the first 6 h as the storm initially develops on the 12-km grid and then show a very rapid intensification between 6-12 h as the simulated storm adjusts to the increased resolution of the 2-km grid. After 14 h, the maximum surface winds exhibit a gradual intensification through 26 h and then a leveling off or slight decrease in the following hours. The simulated maximum surface winds are generally 5-10 m s^{-1} stronger than those observed. This result may be due, in part, to the limited sampling by the aircraft, which would not be expected to sample highly localized wind maxima. However, one would expect the aircraft to, at a minimum, measure wind speeds equal to or greater than the azimuthally averaged values. The azimuthally averaged winds from the model are in excellent agreement with the observed maximum winds suggesting that while the model winds may be stronger than observed, the general trend in the wind speeds is good.

Figure 6 indicates that, after 24 h, the minimum sea-level pressure continues to decrease while the maximum winds level off or weaken slightly. These results are not necessarily inconsistent. Idealized modeling of eyewall mesovortex formation and axisymmetrization by Schubert et al. (1999) and Kossin and Schubert (2001) suggests that pressure can decrease while the maximum winds decrease as a result of the potential vorticity redistribution by horizontal mixing. The regular occurrence of mesovortices (section 5) in the current simulation may be an

indication that a similar process is active here. The role of these eyewall mesovortices in determining the distribution of vertical motion is discussed in section 5 while their role in the exchange of momentum and thermodynamic energy between the eyewall and the eye in Bonnie is reserved for a future paper.

The evolution of the simulated precipitation structure is shown in Fig. 7, where the simulated radar reflectivity[1] field is shown at 6 h intervals. By 18 h (Fig. 7a), 12 h into the 2-km grid simulation, intense precipitation is found on the northeastern side of the eyewall while a precipitation-free area occurs on the southern side. Outer convective rainbands are seen on the northeastern and eastern sides of the storm and very little stratiform precipitation occurs between the eyewall and the outer rainbands. By 24 h (Fig, 7b), the area of precipitation has increased as a significant amount of stratiform precipitation has developed. The heaviest eyewall precipitation remains on the northern and eastern sides of the eyewall. This structure is then maintained for the remainder of the simulation (Figs. 7c, 7d).

The simulated precipitation structure agrees very well with that observed by TRMM during the low-shear period on 22 August (Fig. 3a), but is much less asymmetric than the observed storm during the high-shear period (Fig. 3b). This result suggests that the vertical shear in the model may be weaker than that which occurred over the actual storm on 23 August. Figure 8 shows a time series similar to Fig. 2 showing the area-averaged zonal and meridional winds and the 850-200 hPa vertical wind shear obtained by averaging wind information from the 6-km grid over a circle of radius 300 km. The winds are qualitatively similar to those seen in the ECMWF

analyses. However, the simulated upper-level northwesterly flow is weaker while the low-level southeasterly flow is much stronger. This stronger southeasterly flow is likely associated with much stronger beta gyres in the model than in the analyses. The simulated vertical shear is comparable to that in the analyses on 23-24 August, but attains a significant portion of this magnitude from of the stronger beta gyres. Bender (1997) found that the beta gyres can contribute about 5 m s^{-1} of shear suggesting that about half the shear in Fig. 8c may be associated with the beta gyres. In other words, the nearly steady value of the wind shear after 12 h and the significant contribution of the beta gyres to wind shear suggests that the shear associated with the large-scale environment, which was increasing during this period (Fig. 2c), is not well represented in the simulation. This conclusion is supported by comparisons to simulations of Bonnie by Rogers et al. (2003) and by Zhu et al. (2003). Rogers et al. (2003) estimated 900-400 hPa shear values for 25-26 August with peak values of about 25 m s^{-1} on 25 August decreasing to about 5 m s^{-1} by 27 August, a trend that is consistent with Fig. 2a, but with magnitudes that are much greater. Zhu et al. (2003) simulated 850-200 hPa shear values from 22-26 August with values increasing from 5 to 18 m s^{-1} between 22-24 August and then decreasing back to 5 m s^{-1} by 26 August. Since the vertical wind shear appears to be too weak in the current simulation, the results shown in this study are most applicable to the low-to-moderate shear period of 22 August.

4. Time-averaged structure

In this section, we investigate the time-averaged vertical motion and precipitation distributions and the mechanisms that force wavenumber 1 asymmetries in these fields. Time-

---

[1] The equivalent radar reflectivity factor for any hydrometeor category, Z_x, is computed following Fovell and Ogura (1988) as $Z_x = 720\alpha\kappa N_{0x}\lambda_x^{-7}$, where α is the ratio of the backscattering coefficients for the reflecting particles and water (0.213 for snow and graupel, 1 for rain), $\kappa=10^{18}$, N_{0x} is the intercept parameter of the particle size distribution, λ_x is the slope of the size distribution, $\lambda_x = \left(\pi\rho_x N_x/\rho q_x\right)^{1/4}$, ρ and ρ_x are the densities of air and the hydrometeor

averaged fields for the period 24-30 h are examined. To provide context for how this 6-h period relates to the overall evolution of the simulated storm, Fig. 9 shows the radial and temporal distribution of vertical motion at 5 km. Figure 9a shows the azimuthally averaged vertical motion while Fig. 9b shows the maximum upward motion. Because of the large radius of maximum wind used for the bogus vortex, in the first several hours after the 2-km grid is initialized, the maximum vertical motion occurs at large radius, but rapidly contracts toward smaller radius. By about 15 h, contraction of the vortex slows and the vertical motion becomes concentrated in the eyewall at a radius of about 60 km. After this time, the eyewall continues a slow contraction, reaching a radius of 40 km by the end of the simulation. Between 15-26 h, both the azimuthally averaged vertical motion and the maximum upward motion are relatively strong, which contributes to the gradual intensification of the maximum winds as indicated in Fig. 6b. At about 26.5 h, a final burst of strong convection occurs after which time the azimuthally averaged and maximum upward motions, as well as the maximum winds (Fig. 6b), decrease. The period between 24-30 h contains some of the strongest vertical motions at 5 km and also includes the transition to weaker vertical and tangential circulations.

Figure 10 shows the 6-h averaged fields of vertical motion and total precipitation mixing ratio at four levels from the top of the boundary layer to the upper troposphere. The precipitation contours show that the maximum precipitation occurs on the northeastern side of the storm at all levels. In contrast, the vertical motions show some variation with height. At 1 km (Fig. 10a), the maximum upward motion is on the northeastern side of the storm just inside the region of maximum precipitation. At mid levels (5 and 8 km, Figs. 10b and 10c), the maximum upward motions occur on the southeastern side of the storm, just upstream (in a cyclonic sense) of the

---

type (rain, snow, graupel), respectively, and q_x is the hydrometeor mixing ratio. The reflectivity is expressed in

precipitation maximum. At 12 km (Fig. 10d), the upward motions are much weaker with no clearly defined maximum. Downward motion is strongest at mid-to-upper levels and is concentrated in two areas. The first is on the northwestern side of the storm, just downstream of the precipitation maximum and within or just outside the western portion of the eyewall. The second is within the eye just inside the heavy precipitation associated with the eyewall.

The downdraft structure at the 12 km level on the northwestern side of the storm contains significant fine-scale structure despite the 6-h averaging. A northwest-to-southeast vertical cross section of radial velocity and vertical motion (Fig. 11) indicates that the downdrafts occur in association with a shallow layer of strong inflow immediately beneath a layer of upper-level outflow. The convergence along the interface between the inflow and outflow produces relatively strong downward motion beneath the interface and weak upward motion at upper levels in the eyewall above the interface. Plots of the gradient Richardson number (not shown) at individual times indicate reduced values along this interface in the eyewall and below the inflow outside of the eyewall, with the Richardson number falling below unity just outside of the peak downward motion (25-100 km at 12 km MSL in Fig. 11) as a result of strong vertical shear of the radial wind and very low values of the Brunt-Väisälä frequency. Therefore, the fine-scale structure of the downdrafts in Fig. 10d may be associated with a Kelvin-Helmholtz-type instability. Reasor et al. (2003) noted the development of a local shearing instability in their idealized adiabatic experiments when the imposed shear was sufficiently large (12 m s^{-1}/10 km), but it is unclear whether the instabilities in these cases are caused by similar mechanisms.

The precipitation and vertical motion distribution is very similar to that observed in hurricane Norbert (1984) by Marks et al. (1992), in Hurricane Gloria (1985) by Franklin et al.

---

decibels, or dBZ, where $\mathrm{dBZ} = 10\log_{10}\left(Z_r + Z_s + Z_g\right)$.

(1993), and in hurricanes Jimena (1991) and Olivia (1994) by Black et al. (2002). In each case, upward motion typically occurred upstream of the radar reflectivity maximum and downward motion occurred downstream of the reflectivity maximum. Heymsfield et al (2001) observed strong downward motion (up to -6 m s^{-1}) radially inside the deep convection in the eastern eyewall of Bonnie, values that are comparable to the instantaneous downward motions in the simulation (not shown). Zhu et al. (2003) simulated Bonnie using the MM5 model and suggested that the downward motion at upper levels on the western side of the eyewall was caused by westerly flow associated with the approaching short-wave trough impinging on the western side of the storm. They argued that this flow caused convergence (similar to that implied by Fig. 11) and downward motion that acted to suppress convection in the western eyewall.

The asymmetry of vertical motion and precipitation, however, is not simply a result of suppression of convection on one side of the storm. As discussed in the introduction, many studies have examined the impact of vertical wind shear on the development of wavenumber 1 asymmetries in the eyewall and have described several mechanisms by which this occurs. These include: (1) the tilting of adiabatic vortices by the shear and the subsequent development of upward motion in the downtilt direction as required for the flow to remain balanced (Jones 1995; Wang and Holland 1996a); (2) the subsequent development of upward motion 90 degrees to the right of the tilt direction as a result of the interaction of the vortex flow with the temperature asymmetries generated by (1) (Jones 1995; Wang and Holland 1996a; Frank and Ritchie 1999); and, (3) the effects of flow relative to the storm and an assumed balance between horizontal vorticity advection and vorticity stretching or compression that is generally consistent with upward motion in the downshear direction (Willoughby et al, 1984; Bender 1997; Frank and Ritchie 2001).

Expanding upon mechanism (1), Schecter and Montgomery (2003) and Reasor et al. (2003) examined the tilting of a vortex by shear and found that a damping mechanism intrinsic to the dry adiabatic dynamics suppresses departures from an upright state. This realignment occurs through projection of the tilt asymmetry onto two types of vortex Rossby waves: a quasi-mode, or discrete, vortex Rossby wave and sheared vortex Rossby waves. The former mode is characterized by long-lived precession of the upper part of the tilted vortex relative to the lower part. Initially, the upper vortex is tilted downshear. Subsequently, upward projection of the circulation associated with the low-level vortex causes anticyclonic precession of the upper vortex upshear and eventual realignment, followed by additional cycles of tilting, precession, and realignment. The damping rate of the quasi-mode depends on the characteristics of the vortex, specifically the radial gradient of the potential vorticity (PV) at a critical radius where the precession frequency equals the angular rotation rate of the mean flow. A negative radial PV gradient at the critical radius produces damping, and the stronger the gradient, the faster the damping of the precession. With stronger damping, the vortex achieves a downshear-left equilibrium tilt, while in the limit of no damping, indefinite tilting, precession, and realignment occurs. The sheared vortex Rossby wave mode is characterized by very rapid decay of the tilt and precession as the radial shear of the swirling flow quickly axisymmetrizes the tilt asymmetries.

Before examining the effects of shear on Bonnie's structure, the mean winds and vertical shear in the simulation are described using a hodograph of the storm-relative flow averaged over a circle of radius 300 km (Fig. 12). This wind profile is assumed to be associated with the large-scale environmental flow as well as the effects of the beta gyres. Flow within the boundary layer changes from east-northeasterly near the surface to southeasterly near the top of the boundary

layer (~1 km). Above 1 km, the flow gradually shifts from southeasterly to northwesterly so that the shear vector is northwesterly and has a magnitude of approximately 12 m s^{-1} between 1-12 km.

To investigate the effects of shear-induced vortex tilt, the center position at 8 km was determined at each time following the method outlined in section 3; that is, the centroid of the pressure field was estimated by minimizing its asymmetry. Figure 13 shows the movement of the center at 8 km relative to that at the surface while Fig. 14 shows the azimuthal position of the peak wavenumber 1 upward motion at 5 km as well as the tilt azimuth at 8 km as a function of time for the period 18-36 h. Given the relatively coarse temporal resolution for this period (15 min) and the discrete nature of the center locations (movement in increments of the grid spacing of 2 km), some temporal smoothing has been applied to the results presented in Figs. 13 and 14. The initial 12 hours on the 2-km grid are not shown since this period is strongly influenced by the adjustment of the model to the high-resolution grids (Fig. 9). As indicated in Fig. 14, the maximum wavenumber 1 upward motion occurs on the east-southeastern side of the storm and is clearly occurring in the direction of tilt, a result that demonstrates that mechanism 2 is not active. Variations in the tilt of the vortex at 8 km are generally aligned with variations in the axis of peak wavenumber 1 upward motion at 5 km, providing further support for mechanism 1. An initially large tilt (~12 km, Fig. 13) at 18 h is gradually reduced by half by 26.5 h as the upper center moves through two cyclonic loops. This looping motion of the upper center is consistent with the existence and damping of the quasi-mode of Reasor et al. (2003). During the period of larger tilt, the wavenumber 1 upward motion is strongest. After 26.5 h, the tilt remains relatively small as the storm center at 8 km continues to loop in a generally cyclonic fashion downshear and slightly to the left of the shear vector (Fig. 13). The occurrence of a damped looping motion

of the upper center supports the hypothesis of Reasor et al. (2003) that the mechanism by which hurricane vortices resist tilting by vertical wind shear is governed by the dry adiabatic dynamics and enhanced by the moist physics. A key difference from the results of Reasor et al. (2003) is that in their case of a damped quasi-mode, the equilibrium tilt of the vortex is 90° to the left of the shear vector, while in the Bonnie simulation, the tilt is only slightly to the left of the shear. Wu et al. (2003) describe a simulation of Hurricane Erin (2001) and demonstrate a case in which the tilt direction is up to 90° to the left of the shear and pointing in the direction of the wavenumber 1 upward motion.

As mentioned above, the damping rate of the quasi-mode depends on the radial PV gradient at the vortex critical radius. As described in Schecter and Montgomery (2003) and Reasor et al. (2003), damping of the precession occurs when the radial PV gradient is negative at the critical radius, while a tilt instability (exponentially growing tilt) occurs if the gradient is positive. Figure 15 shows vertical cross sections of the azimuthally and time averaged (hours 24-25) PV and relative vorticity. Superposed on these fields are estimates of the minimum and maximum values of the critical radius where $V/r \sim \omega = 2\pi/T_p$, V is the tangential wind, r is radius, ω is the precession frequency, and T_p is the time required for the center at 8 km to complete one of the loops shown in Fig. 13 (estimated to be between 3-5 h). Since the theoretical work of Reasor et al. (2003) was based upon a barotropic vortex, here we estimate the critical radius using the density-weighted, vertically integrated angular velocity. From Fig. 15a, the critical radius is seen to lie in a region of weak negative PV gradient, so that at least in the context of the theory for an adiabatic vortex, the results are consistent with a damped precession. Moist processes likely accelerate the damping (Reasor et al. 2003) so that the vortex tilt is rapidly reduced between 18-27 h (Fig. 13). The vorticity profile (Fig. 15b) is characterized by a negative radial gradient with negative

relative vorticity developing between 400-500 km (~10 times the radius of maximum winds) at low levels and a possible change in the sign of the gradient further out. This vorticity profile differs from that of Jones (1995) in which the relative vorticity is negative near a radius of 200 km (twice the assumed radius of maximum wind) and the radial gradient of vorticity changes sign near 250 km. Reasor et al. (2003) argue that the critical radius in the Jones (1995) case lies within the region of positive PV gradient so that the Jones profile is associated with a growing tilt asymmetry. Figure 15 suggests that a critical radius within the negative PV gradient region may be more realistic.

Mechanism (3), relative-flow induced vorticity advection and an assumed balance with the stretching or compression of vorticity, is examined by overlaying contours of horizontal divergence with contours of vorticity as well as wind vectors associated with the asymmetric wind (determined by subtracting out the azimuthally averaged tangential and radial winds). According to the vorticity balance argument, areas of negative (positive) vorticity advection should be associated with areas of convergence (divergence). The results (Fig. 16) suggest that this mechanism is at least qualitatively valid since regions with asymmetric inflow (outflow) in the eyewall are associated with convergence (divergence). The relative flow in the boundary layer (Fig. 16a) is from the northeast and the maximum boundary layer convergence occurs on the northeastern side of the eyewall, thereby producing the upward motion maximum there in Fig. 10a. Above the boundary layer, the relative flow is consistent with low-level convergence (Fig. 16b) and upper-level divergence (Fig. 16d) on the southeastern side of the storm, with this divergence pattern producing the maximum upward motion on that side of the eyewall at 5 and 8 km (Figs. 10b, 10c). Interestingly, while the relative flow associated with the shear is readily apparent outside the eyewall at lower and upper levels, the asymmetric flow within the eye is

weak and seemingly unrelated to the relative flow. This result suggests that the eyewall acts as an obstacle to the mean flow and behaves much like a containment vessel, in which the eye air remains since the time it was first enclosed within the eyewall (Willoughby 1998), inhibiting ventilation of the eye by the exterior mean flow.

The simulation has shown that both mechanisms 1 and 3 can account qualitatively for the vertical motion patterns. This result should be expected since both the shear and tilt directions are nearly aligned in this case. With mechanism 1, the shearing wind tilts the vortex and the resultant vertical motion pattern, required by balance constraints, is associated with a divergent flow that consists of low-level convergence and upper-level divergence in the downtilt direction. With mechanism 3, the relative flow associated with the shear produces low-level inflow and convergence and upper-level outflow and divergence on the downshear side of the storm, consistent with an assumed balance between horizontal vorticity advection and the stretching term. Similar results are obtained by Wu et al. (2003) in their simulation of Hurricane Erin (2001).

5. Time-varying structure

Although the time-averaged vertical motion fields show a relatively smoothly varying asymmetric vertical motion pattern, the upward motion in the eyewall at any instant in time is typically comprised of a small number of convective updrafts that occupy only a relatively small percentage of the eyewall area (Jorgensen et al. 1985, Braun 2002, Eastin 2003). In this section, the structure of these updrafts is investigated in much greater detail with emphasis on their formation, vertical structure, and evolution.

The vertical structure and evolution of the updrafts at several different times is indicated in Fig. 17, which overlays contours of upward motion at 1.8, 5.0, and 8.2 km. At 24.4 h (Fig. 17a),

a continuous band of weak upward motion extends around the entire eastern half of the storm at low levels, while more isolated updrafts are seen at mid and upper levels. Here we focus on the updrafts labeled A, B, and C, which at 24.4 h, are located on the southern and western portions of the eyewall. Updraft A extends vertically throughout the troposphere while updrafts B and C are present initially only at upper levels. Twelve minutes later (Fig. 17b), the updrafts have rotated cyclonically about the center. Updraft A remains vertically aligned, updraft B now extends down to near the boundary layer, and updraft C remains present only at upper levels. After another 12 min (Fig. 17c), updraft C also extends down to near the top of the boundary layer. Therefore, during this period, the updrafts appear to form initially at upper levels and then extend down to the boundary layer when they reach the southern side of the eyewall. They are generally vertically aligned with a slight outward tilt, as is common in hurricanes (Jorgensen 1984), so that they can be viewed as deep towers of upward motion rotating about the storm center. An hour later, at 25.8 h (Fig. 17d), updrafts B and C have merged and are now on the northeastern side of the eyewall. New updrafts have formed on the eastern and southern sides of the storm (D, E, and F) and eventually merge (Fig. 17e) to form a well-defined and nearly continuous rainband by 26.4 h. This rainband represents the last burst of convection seen in Fig. 14, and marks the time at which the vortex becomes nearly vertically realigned (Fig. 13), stops intensifying (Fig. 6b), and transitions to a period of weaker vertical motion (Fig. 9b) with fewer, more isolated convective updrafts (Fig. 17f).

In general, the updrafts are observed to form on the southern side and to dissipate on the northern side, similar to the conceptual model of Heymsfield et al. (2001). However, in contrast to their conceptual model, the updrafts are not starting off shallow on the southern side and growing to maximum height on the northern side, but are instead seen to extend through the

depth of the troposphere virtually from their inception. In fact, the updrafts are frequently seen to first develop at mid-to-upper levels (3-8 km) on the southwestern side of the storm and then to extend downward to near the top of the boundary layer on the southern or southeastern side of the storm. This pattern of development can be clearly seen in Fig. 10 by the shift in the location of the upward motion between Fig. 10a and Figs. 10b and 10c. The updrafts reach maximum intensity on the southeastern to eastern side of the eyewall while precipitation growth peaks on the northeastern side.

The statistical distribution of vertical motion in the eyewall can be examined to determine the contribution of the convective updrafts to the total area and condensation within the eyewall. Histograms of updraft area and condensation rate (written directly from the model at 3 min intervals between 24-25 h) as a function of vertical velocity are computed for a 35 km-wide radial band (35-70 km radius) for each model level using a vertical velocity bin size of 0.5 m s^{-1}. The 35-kilometer-wide band just encloses the ensemble of updrafts occurring at all levels in the eyewall during this 1-h period. The shaded contours in Fig. 18 show the cumulative percentage of the eyewall area occupied by updrafts less than the indicated value. Similarly, the solid contours indicate the contribution to the total eyewall condensation produced in updrafts less than the indicated value. The figure indicates that updrafts greater than 2 m s^{-1} occupy somewhat less than 10% of the eyewall area at lower to middle levels and 20% at upper levels. Updrafts greater than 4 m s^{-1} generally occupy less than 5% of the eyewall area, in general agreement with the results of Braun (2002). Although these updrafts account for only a small percentage of the eyewall area, they produce a majority of the total condensation occurring within the eyewall. Updrafts greater than 2 m s^{-1} produce 75% of the total condensation while updrafts greater than 4 m s^{-1} account for half of the condensation.

To explain the mechanisms that control the timing and location of the updrafts, consider the distributions of vorticity, vertical motion, and asymmetric winds shown in Fig. 19. At 1 km (Fig. 19a), an annulus of vorticity contains 4-5 maxima of vorticity, or mesovortices. The strongest mesovortex at this time occurs on the northeastern side of the eyewall and its cyclonic circulation extends up to the 8-km level (Figs. 19d). Considering the two mesovortices on the eastern side of the storm, it can be seen that their circulations produce relative outflow (inflow) on their trailing (leading) sides, where the terms "trailing" and "leading" are defined in terms of the movement of the mesovortices cyclonically around the eyewall. Where the outflow associated with the mesovortices meets with the general area of southeasterly inflow (Figs. 12, 16b, 19a), there is enhanced convergence and in the area of vortex-induced inflow, there is reduced convergence. As a result, the enhanced convergence trailing the mesovortex leads to the formation of the updraft there. This result indicates greater complexity in the relationship between vertical motion and vorticity than expectations from simple Ekman pumping considerations in which the updraft at the top of the boundary layer would be collocated with the mesovortex (Chen and Yau 2001; Fulton 2001). The time-averaged asymmetric flow (Fig. 16) suggested that the eyewall acts as a barrier to the environmental relative flow. The instantaneous fields (Fig. 19) suggest that much of exchange of air between the eye and the environmental air outside the eyewall occurs in association with the eyewall mesovortices (Schubert et al. 1999, Kossin and Schubert 2001, Persing and Montgomery 2003, Eastin 2003).

Further information on the mesovortices is shown in Fig. 20. In Fig. 20a, the absolute vorticity is overlaid on the simulated radar reflectivity, and it can be seen that the mesovortices generally occur along the inner edge of the eyewall reflectivity area. Also apparent is the polygonal shape of the eyewall, in this case forming a square in the reflectivity pattern.

Polygonal eyewalls have been observed by Lewis and Hawkins (1982) to be a frequent occurrence in strong hurricanes. Schubert et al. (1999) and Kossin and Schubert (2001) have shown using idealized simulations that polygonal eyewalls form as a result of the vorticity dynamics of the eyewall. A symmetric annulus of vorticity, representative of the distribution of vorticity within the eyewall of a hurricane, is barotropically unstable. Small perturbations grow rapidly to form mesovortices and polygonal eyewalls. Depending on the initial characteristics of the annulus of vorticity, the mesovortices may mix into the center to form a vortex monopole (Schubert et al. 1999; Kossin and Schubert 2001) or they may form a set of long-lived mesovortices whose number may vary (Kossin and Schubert 2001; Montgomery et al. 2002). Kossin and Schubert (2001) found that monopoles are more likely the form from smaller or radially broader initial vorticity annuli, while stable mesovortices are more likely to form from larger and radially thinner vorticity annuli.

The idealized simulations of Kossin and Schubert (2001) produced local pressure perturbations as low as –25 to –50 hPa in association with the mesovortices. While limited observations of mesovortices are available, the magnitude of the pressure perturbations from Kossin and Schubert (2001) appears to be quite large. Marks and Black (1990) and Black and Marks (1991) described observations taken during a reconnaissance flight through a strong mesovortex in the eyewall of Hurricane Hugo (1989). They estimated the pressure perturbation associated with the mesovortex to be about 12 hPa. Pressure perturbations from the simulation of Bonnie are shown in Fig. 20b and are derived by removing the azimuthal mean pressure field. Relative minima in the perturbation pressure field are associated with each of the mesovortices in the eyewall and have maximum amplitude of about 2.5 hPa. The larger pressure perturbations in the Kossin and Schubert (2001) simulations are likely related to the amplitude of the azimuthally

averaged vorticity used to initialize their simulations. They used vorticity annuli with amplitudes ranging from 22.5-44.8×10^{-3} s^{-1} whereas the simulation of Bonnie produces maximum vorticity values of about 14×10^{-3} s^{-1} and azimuthally averaged values up to 5×10^{-3} s^{-1}.

Marks and Black (1990) and Black and Marks (1991) estimated wind speed perturbations associated with the mesovortex in Hugo to be 20-30 m s^{-1} compared to maximum wind speeds of 90 m s^{-1} and azimuthally averaged winds likely considerably lower. Fulton (2001), in an analysis of the high-resolution simulation of Hurricane Bob (1991) by Braun (2002), found that the maximum tangential winds were consistently 20-30% higher than the azimuthal mean values. Montgomery et al. (2002) showed using laboratory water tank experiments that long-lived mesovortices can produce winds 50% greater than the parent vortex. Wind speed perturbations associated with the mesovortices in Fig. 19a reach up to 15-20 m s^{-1}, so that peak winds (azimuthal mean plus anomalies) at the top of the boundary layer are up to 35% larger than the azimuthally averaged values at the same level.

To demonstrate that this pattern exists at other times, Fig. 21 shows Hovmoller diagrams of the radially averaged (20-54 km) absolute vertical vorticity and vertical velocity at 1.1 and 3.1 km. The vorticity fields show positive vorticity anomalies that rotate around the storm at least once and, in some cases, several times. When these positive vorticity anomalies move into the eastern half of the storm, updrafts form and slightly trail the vorticity anomalies in time in a given direction. Consider vorticity anomaly A in Fig. 21. It starts on the western side of the storm and initiates an updraft when it moves into the eastern side of the storm. It subsequently rotates around the storm, initiates a new burst of convection on the eastern side, and then rotates around again to eventually form a third round of convection. Vorticity anomaly B is associated with at least two episodes of convection before dissipating on the southwestern side of the storm.

Finally, vorticity anomaly C, emerging from an updraft region at 24.5 h, moves around the eyewall and initiates a new updraft near 26 h. On its next passage through the eastern half of the eyewall near 27.8 h, it produces only very weak upward motion in the wake of the burst of convection associated with the organized rainband (Fig. 17e). The vorticity anomaly weakens at 1.1 km just prior to the updraft and at 3.1 km immediately following the updraft. Subsequently, the weakened vorticity anomaly merges with another anomaly (D) and initiates a new updraft at 29.5 h. These results suggest a strong linkage between eyewall mesovortices and convective updrafts. Updrafts form when the mesovortices move into the region where the relative flow supports the upward component of the wavenumber 1 asymmetry in vertical motions. At the same time, the low-level convergence associated with the updrafts modifies the vorticity field so as to maintain the annulus of vorticity and the occasional generation of new mesovortices.

This pattern of updraft development associated with mesovortices is strikingly similar to the tracking of convective cores in hurricanes Jimena (1991) and Olivia (1994) as described by Black et al. (2002). They tracked the positions of reflectivity cores in the eyewalls of these two hurricanes and found a tendency for cell formation to occur on the downshear side and cell dissipation to occur on the upshear side of the eyewall, consistent with the maximum precipitation occurring in the downshear left portion of the eyewall. Furthermore, they noted that clusters of longer-lived cells could be clearly tracked for several orbits around the eyewall, with older cells in the clusters dissipating on the upshear side and newer cells forming on the downshear side. Such behavior is consistent with the presence of long-lived mesovortices as depicted in Fig. 21.

The individual cells and clusters of cells observed by Black et al. (2002) tended to move more slowly than the mean winds in the eyewall, with orbital velocities generally between 56-

72% of the mean flow at the radius of maximum wind. The orbital velocity of the mesovortices in the simulation, estimated from Fig. 21a, is approximately 37 m s^{-1} or approximately 70% of the azimuthal mean flow. The movement of the mesovortices at a speed slower than the mean flow is consistent with expectations for vortex Rossby waves (Montgomery and Kallenbach 1997; Chen and Yau 2001; Fulton 2001).

Given the qualitative understanding that the updrafts form where the mesovortex interacts with the wavenumber 1 forcing of vertical motion associated with vertical wind shear, we are now in a position to explain why the updrafts form at mid levels prior to forming near the top of the boundary layer. Within the boundary layer, the relative asymmetric flow produces maximum convergence on the northeastern side of the eyewall (Fig. 16a) so that the interaction of the mesovortex with this convergence pattern produces updrafts that form on the southeastern side of the storm and dissipate on the northwestern side. In contrast, above the boundary layer, the asymmetric flow produces low-level convergence (Fig. 16b) and upper-level divergence (Fig. 16c) on the southeastern side of the storm, allowing mesovortices to initiate updrafts on the south-southwestern side and later dissipate on the northeastern side of the storm.

6. Conclusions

This study examines the distribution and evolution of vertical motion in a simulation of an asymmetric hurricane. Wind analyses from ECMWF and precipitation data from the TRMM radar suggest that Hurricane Bonnie intensified rapidly and possessed an asymmetric precipitation structure when vertical wind shear was weak to moderate in strength on 22 August, but immediately stopped intensifying and became even more asymmetric as the wind shear increased on 23-24 August. A high-resolution simulation with 2-km grid spacing reproduces well the asymmetric structure of Bonnie during its earlier development on 22 August, but does not

reproduce the highly asymmetric structure of subsequent days since the simulated large-scale wind shear fails to increase as observed. Therefore, results are most applicable to Bonnie's earlier development period.

In agreement with previous simulations (Braun 2002) and observations (Jorgensen et al 1985, Eastin 2003), eyewall upward motions are found to be associated with small-scale convective updrafts that occupy only a small percentage of the eyewall area, but account for a large proportion of the total upward mass flux and condensation. Occasionally, the updrafts occur in sufficient number and proximity that they merge together to form organized rainbands. The updrafts form, intensify, and dissipate on the southern, eastern, and northern sides of the eyewall, respectively. Consequently, when averaged in time, the vertical motion field exhibits a pronounced wavenumber 1 asymmetry with peak upward motion on the northeast side within and near the top of the boundary layer (~1 km) and on the eastern to southeastern side generally above 1.5 km.

Many mechanisms for generating asymmetry as a result of vertical wind shear have been described in the literature. In this case, the peak upward motion in the boundary layer results from convergence in the eyewall where relative inflow occurs in association with the vertical shear. Above the boundary layer, the relative flow produces low-level convergence and upper-level divergence on the southeastern side of the eyewall, leading to the maximum mean upward motion there. These results are consistent with the vorticity balance arguments of Willoughby et al. (1984), Bender (1997) and Frank and Ritchie (2001) in which horizontal advection of vorticity by the relative flow is balanced by stretching or compression of vorticity.

The vertical motion asymmetry is also consistent with the recent findings of Reasor et al (2003). They showed that the tilt of an adiabatic vortex resulting from vertical wind shear can be

projected onto two modes of vortex Rossby waves, sheared waves and a quasi-mode. The latter is associated with precession of the upper vortex relative to the lower vortex such that vertical alignment is maintained and upward motion occurs in the direction of tilt. In the simulation of Bonnie, a 12-km tilt at 18 h is gradually reduced to 3-4 km by 27 h as the upper center undergoes two cyclonic loops (precession cycles). Thereafter, the tilt remains small as the upper center continues its precession in smaller cyclonic loops. The peak of upward motion associated with the wavenumber 1 asymmetry generally lies in the downtilt direction with variations in the direction of the peak coinciding with the direction of tilt associated with the precessing upper vortex. The wavenumber 1 upward motion peak is strongest during the two larger precession loops between 18-26.5 h, and then diminishes for the remainder the simulation as the tilt remains small.

Conceptual models of updrafts in the eyewall envision convective plumes initiating in the boundary layer and rising to the upper troposphere as the updrafts move cyclonically around the eye. The simulation of Bonnie suggests a different picture in which updrafts extend through the depth of the troposphere almost simultaneously upon initiation (in some cases actually forming first at mid-to-upper levels) and then rotate around the eye as vertical columns of rising air. The timing and location of individual updrafts, while seemingly complex, have a surprisingly simple explanation. The updrafts form in association with mesovortices that are produced by the vorticity dynamics of the eyewall. As Schubert et al (1999), Kossin and Schubert (2001), and Montgomery et al (2002) have shown, the annulus of high vorticity associated with the eyewall is barotropically unstable and, under certain conditions, breaks down to form steady mesovortices that rotate around the eye. These mesovortices often give rise to polygonal eyewalls and such structures are clearly evident in the Bonnie simulation. The mesovortices are

relatively deep features that extend from the boundary layer up to 5-8 km. Because of their local cyclonic circulation, mesovortices enhance inflow ahead of and outflow behind their location in the eyewall. The updrafts form in association with the outflow trailing the mesovortices. Specifically, low-level convergence is enhanced where the mesovortex outflow converges with low-level inflow associated with the shear-induced relative flow on the southeastern side of the eyewall. Thus, the timing and location of the updrafts results from an interplay between the mesovortex circulations and the wavenumber 1 forcing of upward motion associated with vertical wind shear.

In this study, we have focused on the distribution of vertical motion and on the role played by eyewall mesovortices in forcing this vertical motion. Mesovortices are also likely important for exchanges of heat and momentum between the eyewall and the eye (Montgomery and Kallenbach 1997, Schubert et al 1999, Kossin and Schubert 2001, Montgomery et al. 2002, Eastin 2003). These processes will be examined using the simulation of Bonnie in a future study.

Acknowledgement: This work was supported by Dr. Ramesh Kakar at NASA Headquarters with funds from the NASA CAMEX-4 program.

Appendix

Changes to the microphysics parameterization scheme were made to reduce problems associated with excessive production of graupel. Comparisons of simulated and observed radar reflectivities and 85 GHz microwave radiances (not shown) suggest that model reflectivities in the ice region were too high and ice scattering signatures in the brightness temperatures were unrealistically low. A major cause of this problem is excessive graupel production in the model.

Modifications to the parameterization were made (and are described below) that, while not solving the problem, do help to reduce it. Additional research toward improving the parameterization will be reserved for future studies.

The production of graupel in the Goddard microphysics scheme generally follows Lin et al. (1983). Sources of graupel include freezing of raindrops, riming of snow, and collection by graupel of rain, cloud water, and snow. Here, we focus on the latter two terms that comprise a major portion of graupel growth. The collection of snow by graupel accounts for a significant amount of graupel production, particularly in areas where updrafts are weak and little or no liquid water is present. For example, in stratiform precipitation regions, this term is often the dominant source for graupel production in the model. However, observations frequently show little or no graupel in stratiform regions because of the lack of liquid water available for riming. The formulation of this term [denoted PGACS, see Eq. 29 of Lin et al. (1983)] expresses the collection efficiency of graupel for snow as

$$E_{GS} = E_1 \exp\left[E_2\left(T - T_0\right)\right], \quad T < T_0 \tag{1}$$

where T is temperature, T_0=273.15 K, E_1=1.0 and E_2=0.09. Figure 4 of Lin et al. (1983) shows estimated values of the collection efficiency that generally do not exceed 0.2 for nearly all temperatures. For this study, we assume that graupel growth from collection of snow is negligible when there is little liquid water available for riming by setting E_1=0 when the sum of cloud and rain liquid water is less than 0.1 g kg^{-1}. Furthermore, when sufficient water is available for riming, the maximum value of the collection efficiency is reduced by setting E_1=0.2. The

impact of this change is to reduce graupel mixing ratios, confine graupel production to the vicinity of active updrafts, and increase the mixing ratio of snow.

The collection of cloud water by graupel is another major source of graupel in updrafts. Excessive graupel production can result from overproduction of supercooled cloud liquid water via the saturation adjustment scheme used to calculate condensation and deposition (Tao et al. 1989). The saturation adjustment scheme assumes that super-saturated conditions lead to condensation and deposition that occur in proportions that depend linearly on temperature between T_{00}=243 and T_0 (Lord et al. 1984),

$$\begin{aligned} \Delta q_c &= -\Delta q_v \left(\frac{T - T_0}{T_0 - T_{00}} \right) \\ \Delta q_i &= -\Delta q_v \left(\frac{T_0 - T}{T_0 - T_{00}} \right) \end{aligned}, \tag{2}$$

where Δq_c, Δq_i, and Δq_v are incremental changes in the mixing ratios of cloud water, cloud ice, and water vapor. This relationship was somewhat arbitrarily chosen and is no more valid than other possible relationships (Lord et al. 1984). Given the high degree of glaciation found in hurricanes (Black and Hallett 1986), it is equally valid to assume relationships that more rapidly transition from condensation to deposition. In this study, we assume that the proportions of cloud water and ice produced by condensation and deposition depend exponentially on temperature following (1) with E_1=1, E_2=0.2, and

$$\begin{aligned} \Delta q_c &= -\Delta q_v \exp\left[E_2 (T - T_0) \right] \\ \Delta q_i &= -\Delta q_v \left\{ 1 - \exp\left[E_2 (T - T_0) \right] \right\} \end{aligned}. \tag{3}$$

The impact of this change is to decrease (increase) cloud liquid water (cloud ice) above the melting level and subsequently reduce graupel and increase snow mixing ratios. The changes have little impact on the results presented in sections 4 and 5, but are included here for completeness.

References

Bender, M. A., 1997: The effect of relative flow on the asymmetric structure in the interior of hurricanes. *J. Atmos. Sci.*, **54**, 703-724.

Bister, M. and K. A. Emanuel, 1998: Dissipative heating and hurricane intensity. *Meteor. Atmos. Phys.*, **55**, 233-240.

Black, M. L., J. F. Gamache, F. D. Marks, Jr., C. E. Samsury, and H. E. Willoughby, 2002: Eastern Pacific Hurricanes Jimena of 1991 and Olivia of 1994: The effect of vertical shear on structure and intensity. *Mon. Wea. Rev.*, **130**, 2291-2312.

Black, P. G., and F. D. Marks, Jr., 1991: The structure of an eyewall mesovortex in Hurricane Hugo (1989). Preprints, *19th Conf. on Hurricanes and Tropical Meteorology*, Miami, FL, Amer. Meteor. Soc., 579-582.

Black, R. A., and J. Hallett, 1986: Observations of the distribution of ice in hurricanes. *J. Atmos. Sci.*, **43**, 802-822.

Braun, S. A., 2002: A cloud-resolving simulation of Hurricane Bob (1991): Storm structure and eyewall buoyancy. *Mon. Wea. Rev.*, **130**, 1573-1592.

Chen, Y., and M. K. Yau, 2001: Spiral bands in a simulated hurricane. Part I: Vortex Rossby wave verification. *J. Atmos. Sci.*, **58**, 2128-2145.

Corbosiero, K. L., and J. Molinari, 2003: The Relationship between Storm Motion, Vertical Wind Shear, and Convective Asymmetries in Tropical Cyclones, *J. Atmos. Sci.*, **60**, 366-376.

Dudhia, J, 1989: Numerical study of convection observed during the winter monsoon experiments using a mesoscale two-dimensional model. *J. Atmos. Sci.*, **46**, 3077-3107.

———, 1993: A nonhydrostatic version of the Penn State-NCAR mesoscale model: Validation tests and simulation of an Atlantic Cyclone and cold front. *Mon. Wea. Rev.*, **121**, 1493-1513.

Eastin, M. D., 2003: Buoyancy of convective vertical motions in the inner core of intense hurricanes. Atmos. Sci. Paper No. 744, Dept. Atmospheric Sci., Colorado State University, 160 pp. (available from Dept. Atmospheric Sci., Colorado State University, Fort Collins, CO 80523).

Flatau, M., W. H. Schubert, and D. E. Stevens, 1994: The role of baroclinic processes in tropical cyclone motion: The influence of vertical tilt. *J. Atmos. Sci.*, **51**, 2589-2601.

Fovell, R. G., and Y. Ogura, 1988: Numerical simulation of a midlatitude squall line in two dimensions. *J. Atmos. Sci.*, **45**, 3846-3879.

Frank, W. M., and E. A. Ritchie, 1999: Effects of environmental flow upon tropical cyclone structure. *Mon. Wea. Rev.*, **12**, 2044-2061.

———— and ————, 2001: Effects of vertical wind shear on the intensity and structure of numerically simulated hurricanes. *Mon. Wea. Rev.*, **129**, 2249-2269.

Franklin, J. L., S. J. Lord, S. E. Feuer, and F. D. Marks, Jr., 1993: The kinematic structure of Hurricane Gloria (1985) determined from nested analyses of dropwindsonde and Doppler radar data. *Mon. Wea. Rev.*, **121**, 2433-2451.

Fulton, J. D., 2001: Insights into the hurricane vortex using a high-resolution simulation of Hurricane Bob (1991). Master Thesis, Colorado State University, 84 pp.

Garratt, J. R., 1992: *The Atmospheric Boundary Layer*, Cambridge University Press, 316 pp.

Grell, G. A., J. Dudhia, and D. R. Stauffer, 1995: A description of the fifth-generation Penn State/NCAR Mesoscale Model (MM5). NCAR Technical Note (NCAR/TN-398+STR), 122 pp.

Heymsfield, G. M., J. Halverson, J. Simpson, L. Tian, and T. P. Bui, 2001: ER-2 Doppler radar (EDOP) investigations of the eyewall of Hurricane Bonnie during CAMEX-3. *J. Appl. Meteor.*, **40**, 1310-1330.

Holland, G.,1980:An analytic model of the wind and pressure profile in hurricanes. *Mon. Wea. Rev.*, **108**, 1212-1218.

Jones, S. C., 1995: The evolution of vortices in vertical shear: Initially barotropic vortices. *Quart. J. Roy. Meteor. Soc.*, **121**, 821-851.

Jorgensen, D. P., 1984: Mesoscale and convective-scale characteristics of mature hurricanes. Part II: Inner core structure of Hurricane Allen (1980). *J. Atmos. Sci.*, **41**, 1287-1311.

———, E. J. Zipser, and M. A. LeMone, 1985: Vertical motions in intense hurricanes. *J. Atmos. Sci.*, **42**, 839-856.

Kossin, J. P. and W. H Schubert, 2001: Mesovortices, polygonal flow patterns, and rapid pressure falls in hurricane-like vortices. *J. Atmos. Sci.*, **58**, 2196-2209.

Kurihara, Y., M. A. Bender and R. J. Ross, 1993: An initialization scheme of hurricane models by vortex specification. *Mon. Wea. Rev.*, **121**, 2030-2045.

Lewis, B. M., and H. F. Hawkins, 1982:Polygonal eye walls and rainbands in hurricanes. *Bull. Amer. Meteor. Soc.*, **63**, 1294-1300.

Lin, Y.-L., R. D. Farley, and H. D. Orville, 1983: Bulk parameterization of the snow field in a cloud model. *J. Climate Appl. Meteor.*, **22**, 1065-1092.

Lord, S. J., H. E. Willoughby, and J. M. Piotrowicz, 1984: Role of a parameterized ice-phase microphysics in an axisymmetric nonhydrostatic tropical cyclone model. *J. Atmos. Sci.*, **41**, 2836-2848.

Manning, K. W., and P. L. Haagenson, 1992: Data ingest and objective analysis for the PSU/NCAR modeling system: Programs DATAGRID and RAWINS. NCAR Technical Note (NCAR/TN-376+IA), 209 pp.

Marks, F., Jr., 1985: Evolution of the structure of precipitation in Hurricane Allen (1980). *Mon. Wea. Rev.*, **113**, 909-930.

————, and P. G. Black, 1990: Close encounter with an intense mesoscale vortex within Hurricane Hugo (September 15, 1989). *Fourth Conf. on Mesoscale Processes*, Boulder, CO, Amer. Meteor. Soc., 114-115.

————, R. A. Houze, Jr., and J. F. Gamache, 1992: Dual-aircraft investigation of the inner core of Hurricane Norbert. Part I: Kinematic structure. *J. Atmos. Sci.*, **49**, 919-942.

Mlawer, E. J., S. J. Taubman, P. D. Brown, M. J. Iacono, and S. A. Clough, 1997: Radiative transfer for inhomogeneous atmosphere: RRTM, a validated correlated-k model for the longwave. *J. Geophys. Res.*, **102 (D14)**, 16663-16682.

Montgomery, M. T., and R. J. Kallenbach, 1997: A theory for vortex Rossby waves and its application to spiral bands and intensity changes in hurricanes. *Quart. J. Roy. Meteor. Soc.*, **123**, 435-465.

————, V. A. Vladimirov, and P. V. Denissenko, 2002: An experimental study on hurricane mesovortices. *J. Fluid Mech.*, **471**, 1-32.

Pagowski, M., and G. W. K. Moore, 2001: A numerical study of an extreme cold-air outbreak over the Labrador Sea: Sea Ice, air-sea interaction, and development of polar lows. *Mon. Wea. Rev.*, **129**, 47-72.

Persing, J., and M. T. Montgomery 2003: Hurricane superintensity. *J. Atmos. Sci.*, **60**, 2349-2371.

Pu, Z., and S. Braun, 2001: Evaluation of bogus vortex techniques with four-dimensional variational data assimilation. *Mon. Wea. Rev.*, **129**, 2023-2039.

Raymond, D. J., 1992: Nonlinear balance and potential-vorticity thinking at large Rossby number. *Quart. J. Roy. Meteor. Soc.*, **118**, 987-1015.

Reasor, P. D., and M. T. Montgomery, 2001: Three-dimensional alignment and corotation of weak, TC-like vortices via linear vortex Rossby waves. *J. Atmos. Sci.*, **58**, 2306-2330.

————, ————, and L. D. Grasso, 2003: A new look at the problem of tropical cyclones in vertical shear flow: Vortex resiliency. *J. Atmos. Sci.*, (submitted).

Rogers, R, S. Chen, J. Tenerelli, and H. Willoughby, 2003: A numerical study of the impact of vertical shear on the distribution of rainfall in Hurricane Bonnie (1998), *Mon. Wea. Rev.*, **131**, 1577-1599.

Schecter, D. A., and M. T. Montgomery, 2003: On the symmetrization rate of an intense geophysical vortex. *Dyn. Atmos. and Oceans*, **37**, 55-88.

Schubert, W. H., M. T. Montgomery, R. K. Taft, T. A. Guinn, S. R. Fulton, J. P. Kossin, and J. P. Edwards, 1999: Polygonal eyewalls, asymmetric eye contraction, and potential vorticity mixing in hurricanes. *J. Atmos. Sci.*, **56**, 1197-1223.

Shapiro, L. J., 1983: The asymmetric boundary layer flow under a translating hurricane. *J. Atmos. Sci.*, **40**, 1984-1998.

Tao, W.-K., J. Simpson, and M. McCumber, 1989: An ice-water saturation adjustment. *Mon. Wea. Rev.*, **117**, 231-235.

Wang, B., and X. Li, 1992: The beta drift of three-dimensional vortices: A numerical study. *Mon. Wea. Rev.*, **120**, 579-593.

Wang, Y., and G. J. Holland, 1996a: The beta drift of baroclinic vortices. Part I: Adiabatic vortices. *J. Atmos. Sci.*, **53**, 411-427.

——— and ———, 1996b: Tropical cyclone motion and evolution in vertical shear. *J. Atmos. Sci.*, **53**, 3313-3332.

——— and ———, 1996c: The beta drift of baroclinic vortices. Part II: Diabatic vortices. *J. Atmos. Sci.*, **53**, 3737-3756.

Willoughby, H. E., 1998: Tropical cyclone eye thermodynamics. *Mon. Wea. Rev.*, **126**, 3053-3067.

———, F. D. Marks, Jr., and R. J. Feinberg, 1984: Stationary and moving convective bands in hurricanes. *J. Atmos. Sci.*, **41**, 3189-3211.

Xiao, Q, X. Zou, and B. Wang, 2000: Initialization and simulation of a landfalling hurricane using variational bogus data assimilation scheme. *Mon. Wea. Rev.*, **187**, 2252-2269.

Zhang, D.-L., and E. Altshuler, 1999: The effects of dissipative heating on hurricane intensity. *Mon. Wea. Rev.*, **127**, 3032-3038.

Zhu, T., D.-L. Zhang, and F. Weng, 2003: Numerical simulation of hurricane Bonnie (1998). Part I: Eyewall evolution and intensity changes. *Mon. Wea. Rev.*, (submitted).

Zou, X., and Q. Xiao, 2000: Studies on the initialization and simulation of a mature hurricane using a variational bogus data assimilation scheme. *J. Atmos. Sci.*, **57**, 836-860.

FIGURE CAPTIONS

Figure 1. Geopotential height and wind vectors at (a, c) 850 hPa and (b, d) 200 hPa. Upper panels (a, b) are for 1200 UTC 22 August 1998 while lower panels (c, d) are for 1200 UTC 24 August. Contour intervals are 2 dam at 850 hPa and 5 dam at 200 hPa. Wind vector scales are shown in the upper left corner of each panel. In (a, c), Bonnie's observed track is indicated by the thick solid line with circles drawn every 12 h and dates provided at 00 UTC of each day up until the time of landfall.

Figure 2. Time series of (a) zonal wind, (b) meridional wind, and (c) 850-200 mb vertical wind shear (solid line) and minimum sea-level pressure (dashed line). Wind information was obtained by averaging ground-relative wind fields from 1°-resolution ECMWF analyses over a 5°-radius circle centered on the storm. Positive (negative) values are indicated by solid (dashed) lines. Contour intervals in (a) and (b) are 2 m s^{-1}. Vertical lines indicate the times of two TRMM overpasses shown in Fig. 3. Minimum sea-level pressure was obtained from best-track estimates.

Figure 3. Radar reflectivity at 2 km above mean sea level (MSL) from the TRMM precipitation radar for (a) 1800 UTC 22 August and (b) 1050 UTC 24 August.

Figure 4. Map of the coarse- and fine-mesh domains. The finest 2-km grid is moved with the storm, but only its initial position is shown. Tick marks for the outer 36-km grid and inner 12-km grid are drawn every 5 grid points.

Figure 5. Comparison of the observed (solid line with triangles) and simulated (diamonds) tracks. Symbols are drawn at 6-h intervals starting at 1200 UTC 22 August. Numerical values of track error are provided in the inset table.

Figure 6. Comparison of the observed (thick solid lines) and simulated (thin lines) intensity as measure by (a) the minimum sea-level pressure and (b) the maximum surface wind speed. In (b), the thin solid line is the maximum wind speed at the lowest model level while the thin dashed line is the maximum azimuthally averaged wind at that level. The thick solid line is the maximum surface wind estimated by reconnaissance aircraft. Results from the first 6 h are from the 12-km grid and for the remainder of the simulation are from the 2-km grid.

Figure 7. Simulated radar reflectivity at 1 km MSL at (a) 18 h, (b) 24 h, (c) 30 h, and (d) 36 h. Shaded contours are drawn at 20, 30, 40, and 50 dBZ.

Figure 8. Time series of (a) zonal wind, (b) meridional wind, and (c) 850-200 mb vertical wind shear. Wind information was obtained by averaging ground-relative wind fields from the 6-km grid over a 300-km-radius circle centered on the storm. Positive (negative) values are indicated by solid (dashed) lines. Contour intervals in (a) and (b) are 2 m s^{-1}.

Figure 9. Time-radius distributions of (a) azimuthally averaged vertical velocity and (b) maximum vertical velocity at 5 km. The contour interval in (a) is 0.4 m s^{-1} with the zero contour highlighted by the thick solid contour and in (b) is 2.5 m s^{-1} starting at 2.5 m s^{-1}. Horizontal lines bracket the period for which time-averaged quantities are obtained.

Figure 10. Time-averaged total precipitation mixing ratio (shading; sum of rain, snow, and graupel) and vertical velocity (contours). Precipitation contours are at 0.5, 1, 2, 3, and 4 g kg^{-1}. Vertical velocity contours are at intervals of 0.75 m s^{-1} for updrafts (thick solid lines) and 0.25 m s^{-1} for downdrafts (thin solid lines). The zero contour is indicated by dotted lines. Panels show fields at (a) 1.1 km, (b) 5.0 km, (c) 8.2 km, and (d) 12.0 km. The solid line in (d) indicates the location of the vertical cross section in Fig. 11, which extends somewhat beyond the boundaries of the plot in (d).

Figure 11. Vertical cross section of time-averaged vertical (shading) and radial velocity (contours) along the line indicated in Fig. 10d. Vertical velocity contours are drawn at 0.25 m s^{-1} for downdrafts and 0.5 m s^{-1} for updrafts. The thin solid contour indicates upward motions greater than 0.5 m s^{-1}. Radial velocities are relative to the time-averaged center location at each height and are drawn at 3 m s^{-1} intervals with positive (negative) values are indicated by solid (dashed) lines.

Figure 12. Hodograph of the storm-relative flow from the 6-km grid averaged over a circle of radius 300 km. Diamonds and numbers indicate the heights of the model levels in kilometers.

Figure 13. Displacement of the storm center at 8.2 km from the surface center. Time is indicated by the numbers while the line gets thicker and darker with time. The arrow indicates the direction of the shear vector for the layer between 1.1-12 km MSL.

Figure 14. Time-azimuth distribution of wavenumber 1 vertical motion showing updraft contours at an interval of 0.25 m s^{-1} with the zero contour indicated by the dotted line. The dashed line shows the axis of peak wavenumber 1 upward motion. The solid line shows the direction of vortex tilt, with the thickness of the line proportional to vortex tilt (thicker for larger tilt). The solid vertical line indicates the direction of the shear vector.

Figure 15. Vertical cross sections of the time-averaged (24-25 h) potential vorticity in (a) and relative vorticity in (b). Contours for PV are drawn at –1, –0.5, 0, 0.25, 0.5, 0.75, 1, 1.5, 2, 4, 6, 9, 12, 15 and 20 PV units (10^{-6} m^2 s^{-1} K kg^{-1}). Negative values are indicated by black shading, positive values by increasingly darker gray shades at 0.5, 2, and 12 PV units. Contours of relative vorticity are at –0.1, –0.05, 0, 0.05, 0.1, 0.15, 0.2, 0.25, 0.5, 0.75, 1, 1.5, 2, and 2.5×10^{-3} s^{-1}. Negative values are indicated by white, positive values by increasingly darker gray shades at 0, 0.1, and 0.5×10^{-3} s^{-1}. Solid straight lines indicate the range of estimated radii where value of the precession frequency equals the density-weighted, vertically integrated angular velocity.

Figure 16. Absolute vertical vorticity (shading), divergence (contours), and asymmetric winds (vectors). Vorticity contours are at 1, 2, 3, and 4×10^{-3} s^{-1}. Divergence contours are at 0.5×10^{-3} s^{-1} intervals, with the zero contour omitted. Positive (negative) values are indicated by solid (dashed) lines. The asymmetric winds are relative to the time-averaged center position at each height. The vector scale is indicated above the upper-left corner. Panels show fields at (a) 0.25 km, (b) 1.1 km, (c) 5.0 km, and (d) 9.9 km.

Figure 17. Vertical velocity at 1.9, 5.0 , and 8.2 km. Shading shows updrafts at 1.9 km MSL at contour levels of 1.5, 3, 4.5, and 6 m s^{-1}. Thick gray contours show updrafts at 5.0 km while thin dark contours show updrafts at 8.2 km at values of 3, 6, 9, and 12 m s^{-1}. The time corresponding to each panel is shown in the upper-left corner. Letters indicate updrafts discussed in the text.

Figure 18. Shading indicates the cumulative frequency of the percentage of the eyewall area occupied by updrafts less than the indicated value. Contours are drawn at 10% intervals, with additional contours at 95 and 99%. Thick lines show the cumulative frequency of total eyewall condensation occurring in updrafts less than the indicated values.

Figure 19. Absolute vorticity (shading), vertical velocity (contours, updrafts only), and storm-relative asymmetric wind vectors at 25.6 h at (a) 1.1 km, (b) 3.1 km, (c) 5.0 km, and (d) 8.2 km MSL. Contour interval for vorticity is 1×10^{-3} s^{-1}. Contours of vertical motion are at 1.5 m s^{-1} intervals starting at 1.5 m s^{-1}. Asymmetric wind vectors are obtained by subtracting the azimuthally averaged radial and tangential winds. The vector scale is indicated above the upper-left corner of each panel.

Figure 20. (a) Simulated radar reflectivity (shading) and absolute vorticity at 25.6 h and 1 km MSL. Contour interval for vorticity is 1×10^{-3} s^{-1}. (b) Absolute vorticity (shading) and pressure perturbation (contours). Pressure perturbation is obtained by subtracting the azimuthal mean pressure. Contour interval is 0.5 hPa. In (a) and (b), positive (negative) values are indicated by solid (dashed) lines.

Figure 21. Time-azimuth distributions of radially averaged (20-54 km) absolute vorticity (shading, contour interval of 0.25×10^{-3} s^{-1} starting at 1.25×10^{-3} s^{-1}) and vertical velocity (contours, 0.1 m s^{-1} intervals starting at 0.6 m s^{-1}) at (a) 1.1 km and (b) 3.1 km. The plot has been extended to three revolutions around the center. Solid lines follow individual vorticity disturbances, or mesovortices, at 1.1 km and are also overlaid on the 3.1 km fields for comparison. Letters label features described in the text and are unrelated to similar labeling in Fig. 17.

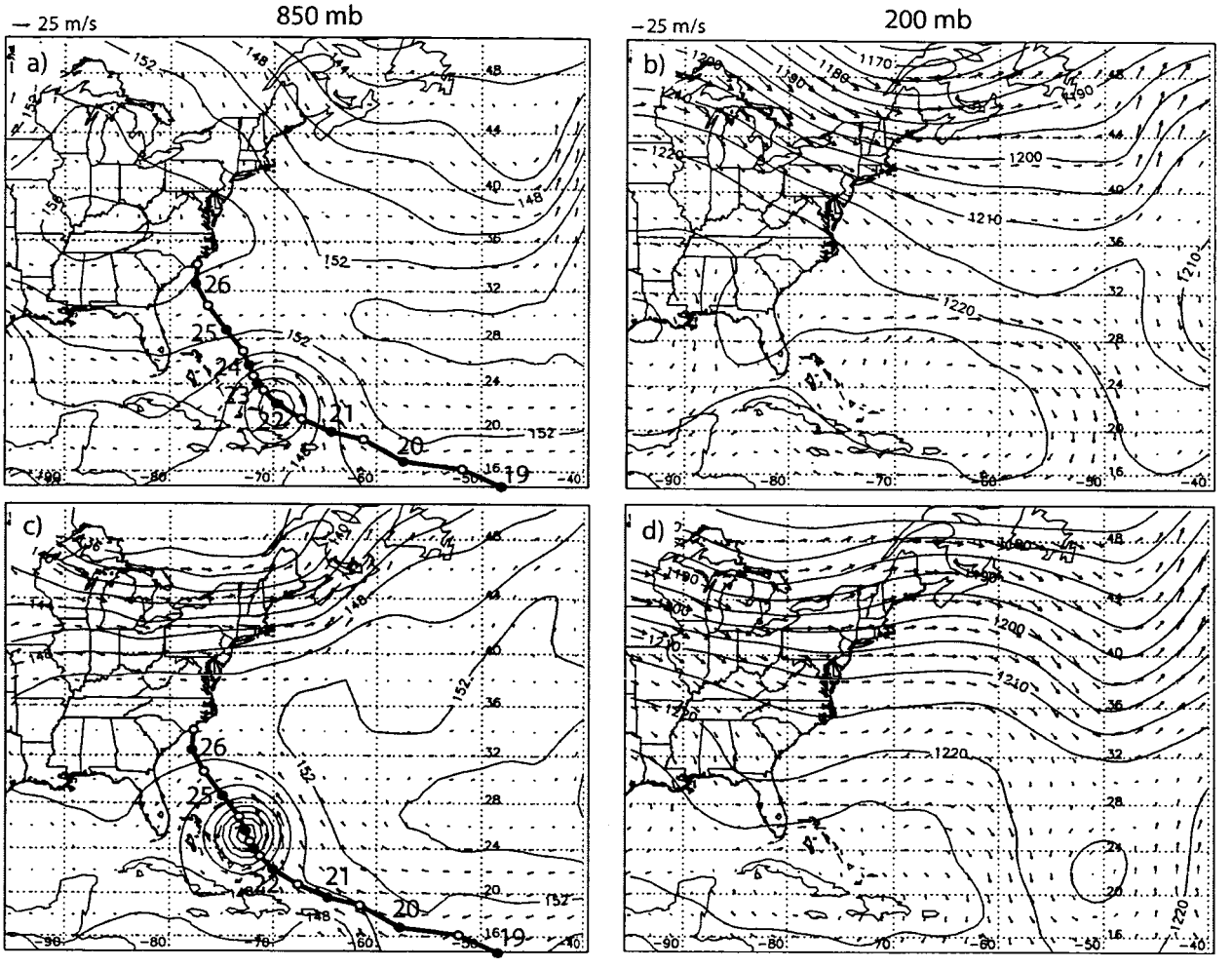

Figure 1. Geopotential height and wind vectors at (a, c) 850 hPa and (b, d) 200 hPa. Upper panels (a, b) are for 1200 UTC 22 August 1998 while lower panels (c, d) are for 1200 UTC 24 August. Contour intervals are 2 dam at 850 hPa and 5 dam at 200 hPa. Wind vector scales are shown in the upper left corner of each panel. In (a, c), Bonnie's observed track is indicated by the thick solid line with circles drawn every 12 h and dates provided at 00 UTC of each day up until the time of landfall.

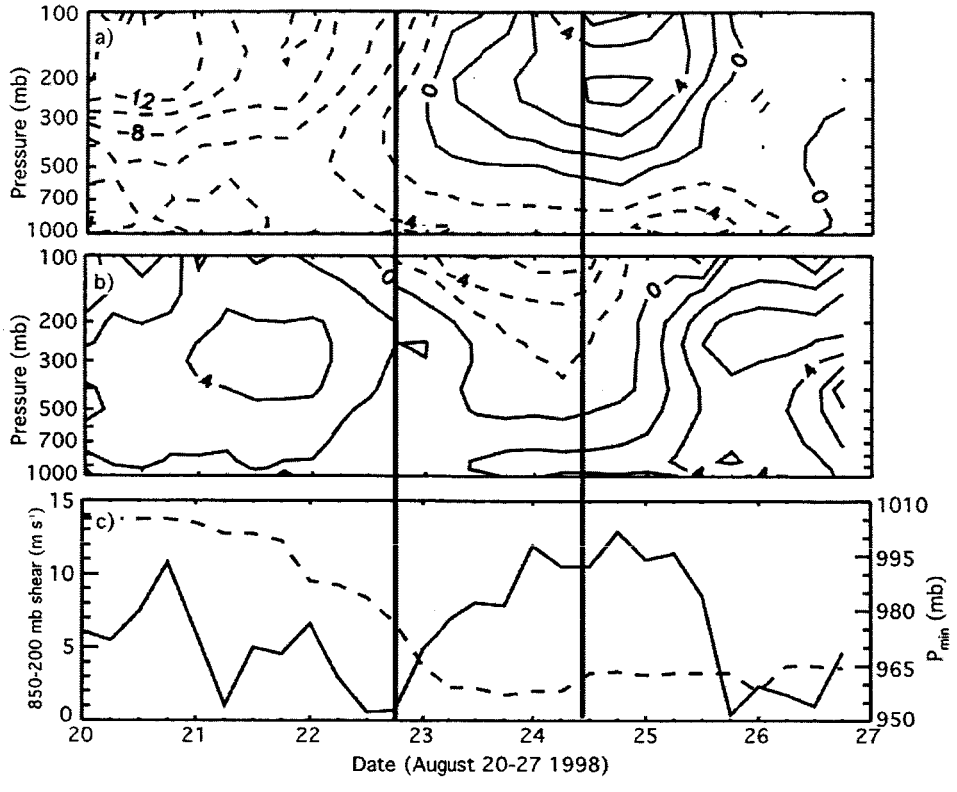

Figure 2. Time series of (a) zonal wind, (b) meridional wind, and (c) 850-200 mb vertical wind shear (solid line) and minimum sea-level pressure (dashed line). Wind information was obtained by averaging ground-relative wind fields from 1°-resolution ECMWF analyses over a 5°-radius circle centered on the storm. Positive (negative) values are indicated by solid (dashed) lines. Contour intervals in (a) and (b) are 2 m s^{-1}. Vertical lines indicate the times of two TRMM overpasses shown in Fig. 3. Minimum sea-level pressure was obtained from best-track estimates.

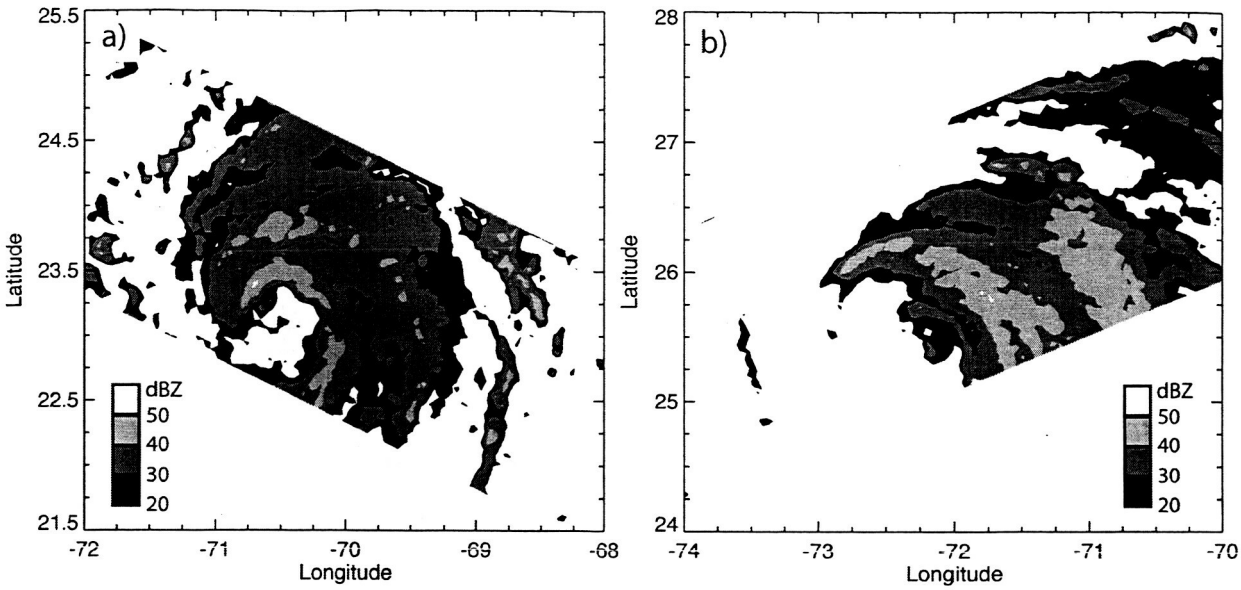

Figure 3. Radar reflectivity at 2 km above mean sea level (MSL) from the TRMM precipitation radar for (a) 1800 UTC 22 August and (b) 1050 UTC 24 August.

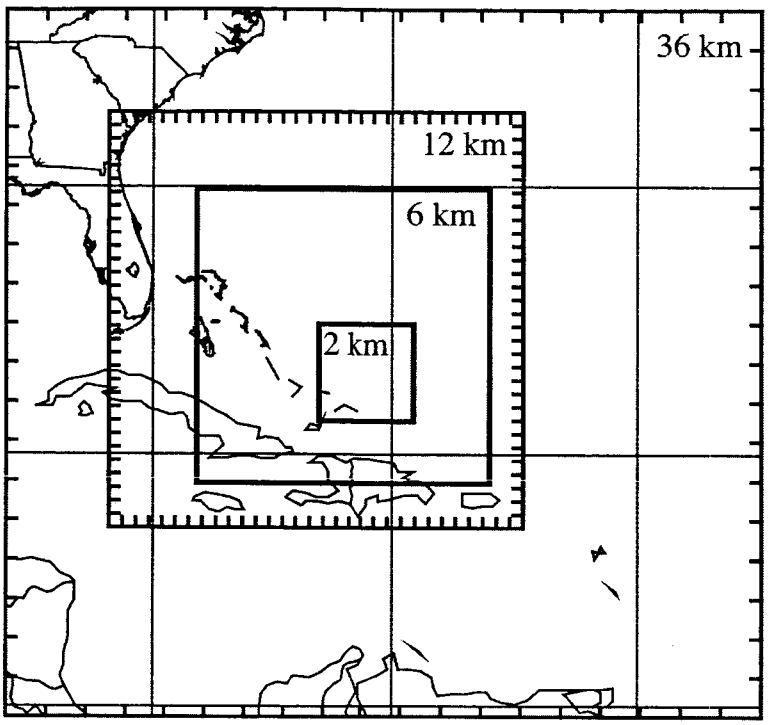

Figure 4. Map of the coarse- and fine-mesh domains. The finest 2-km grid is moved with the storm, but only its initial position is shown. Tick marks for the outer 36-km grid and inner 12-km grid are drawn every 5 grid points.

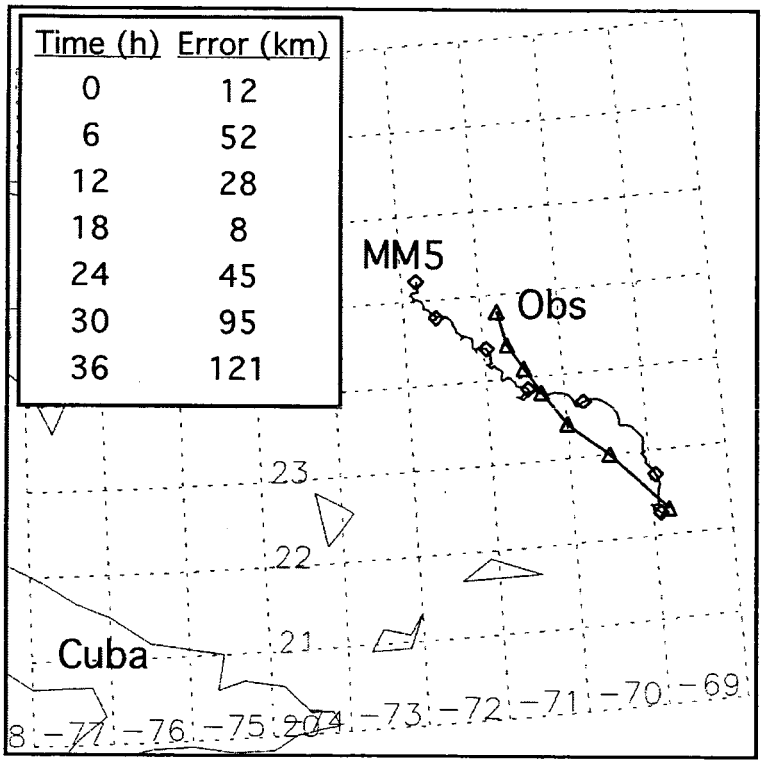

Figure 5. Comparison of the observed (solid line with triangles) and simulated (diamonds) tracks. Symbols are drawn at 6-h intervals starting at 1200 UTC 22 August. Numerical values of track error are provided in the inset table.

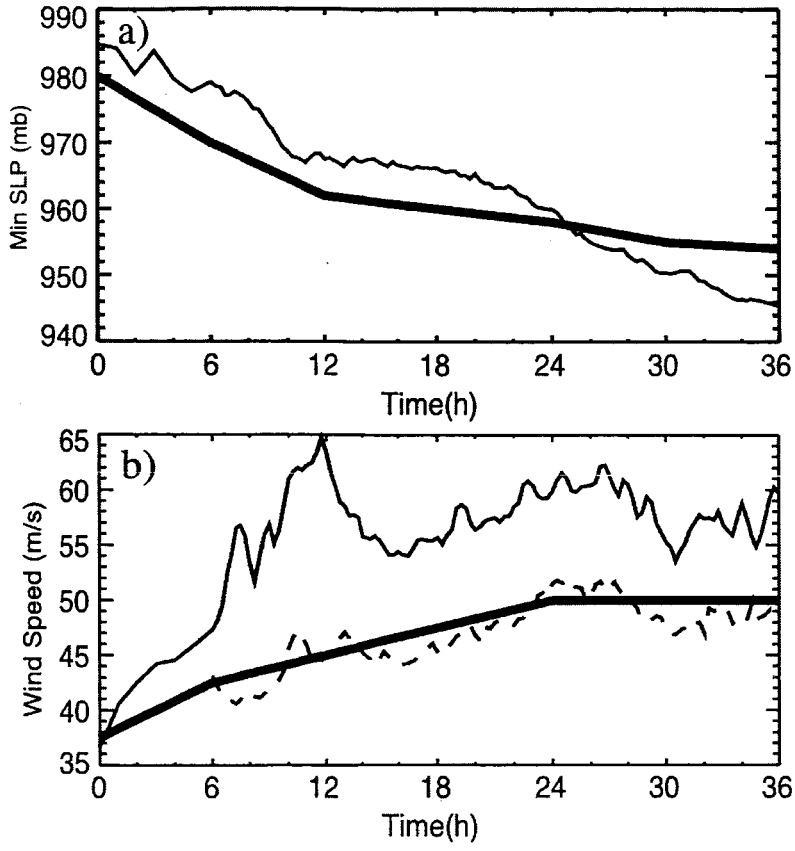

Figure 6. Comparison of the observed (thick solid lines) and simulated (thin lines) intensity as measure by (a) the minimum sea-level pressure and (b) the maximum surface wind speed. In (b), the thin solid line is the maximum wind speed at the lowest model level while the thin dashed line is the maximum azimuthally averaged wind at that level. The thick solid line is the maximum surface wind estimated by reconnaissance aircraft. Results from the first 6 h are from the 12-km grid and for the remainder of the simulation are from the 2-km grid.

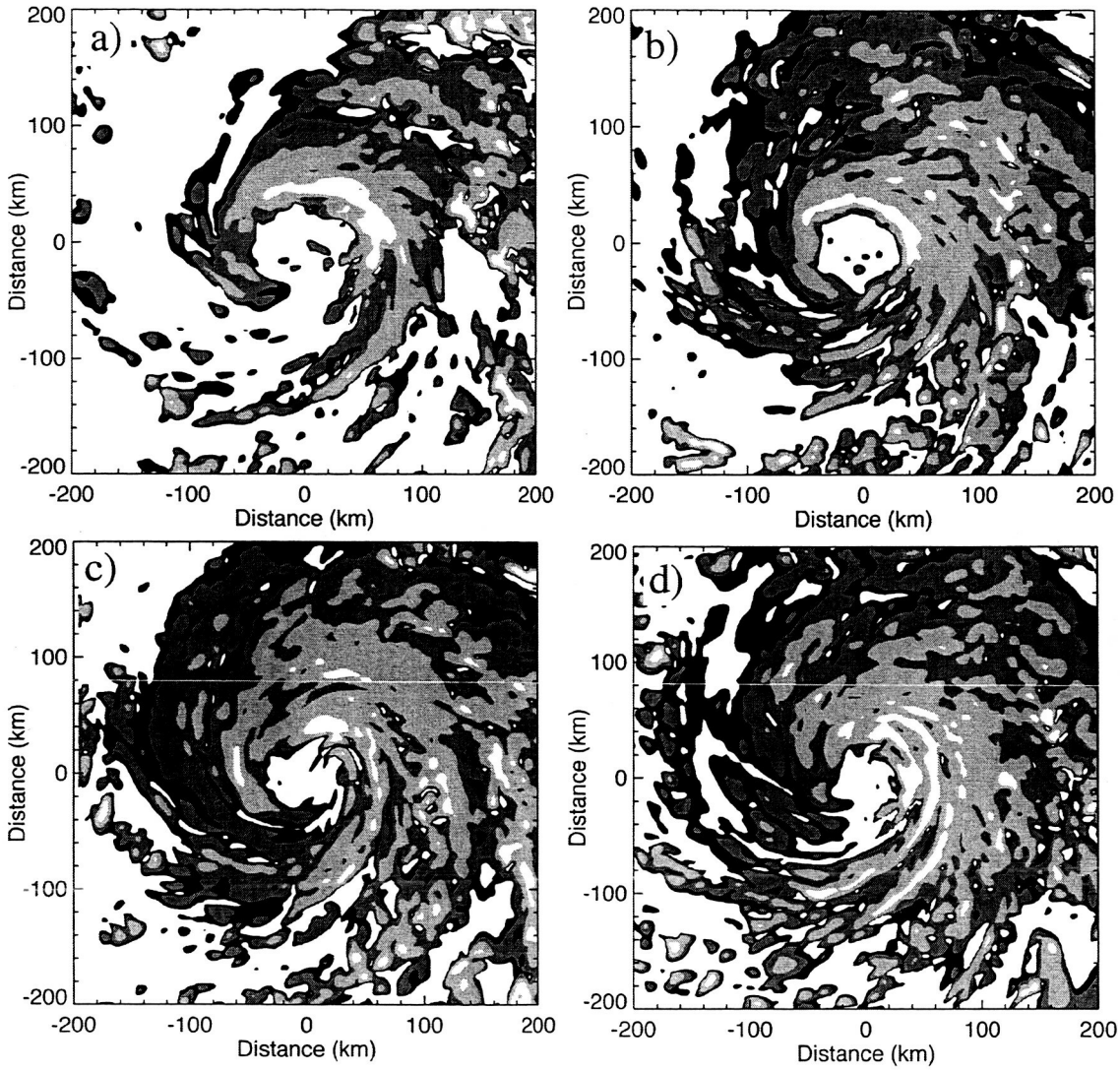

Figure 7. Simulated radar reflectivity at 1 km MSL at (a) 18 h, (b) 24 h, (c) 30 h, and (d) 36 h. Shaded contours are drawn at 20, 30, 40, and 50 dBZ.

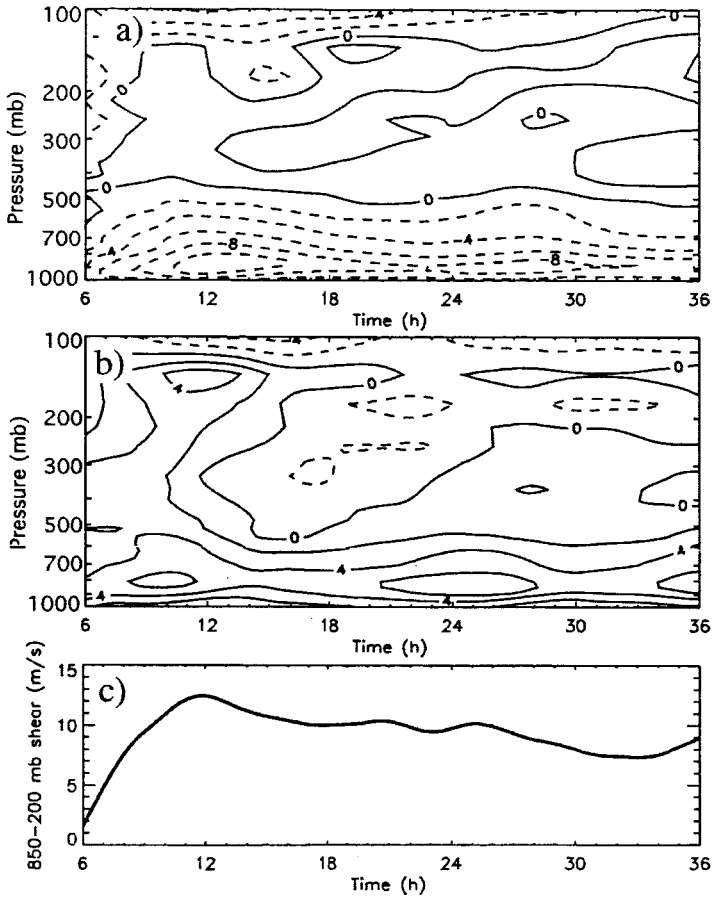

Figure 8. Time series of (a) zonal wind, (b) meridional wind, and (c) 850-200 mb vertical wind shear. Wind information was obtained by averaging ground-relative wind fields from the 6-km grid over a 300-km-radius circle centered on the storm. Positive (negative) values are indicated by solid (dashed) lines. Contour intervals in (a) and (b) are 2 m s^{-1}.

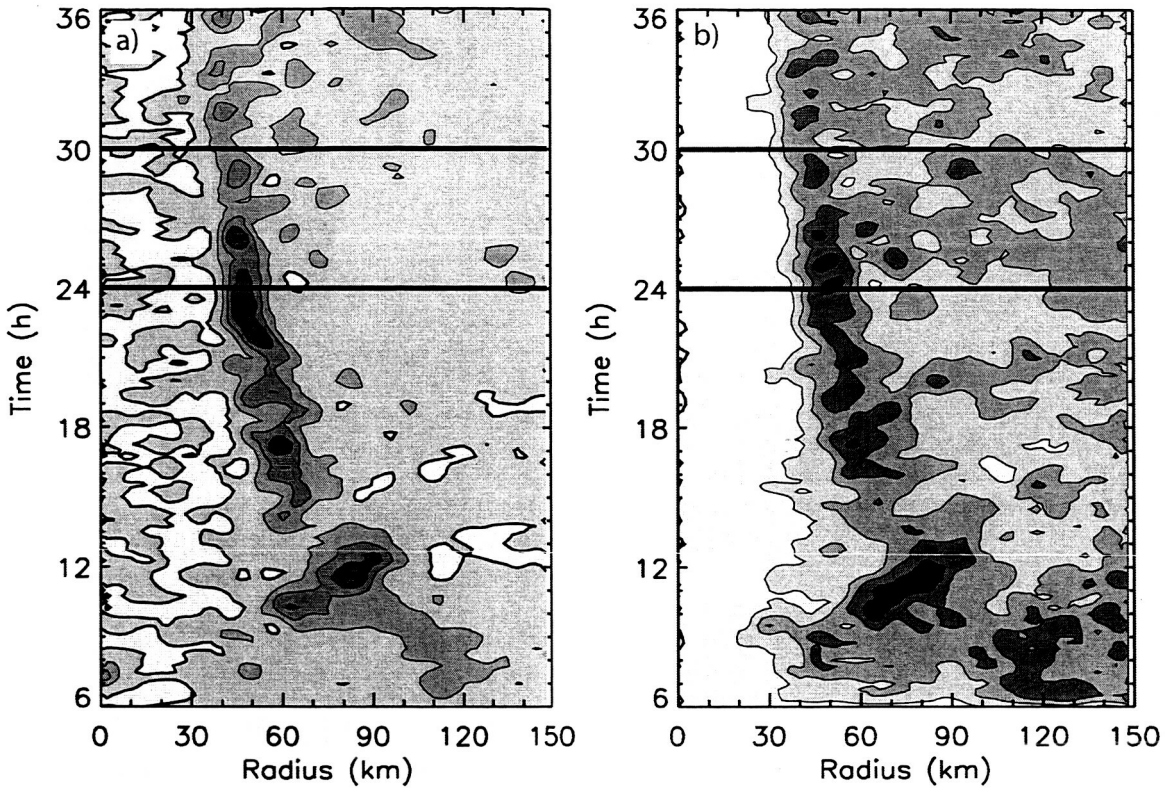

Figure 9. Time-radius distributions of (a) azimuthally averaged vertical velocity and (b) maximum vertical velocity at 5 km. The contour interval in (a) is 0.4 m s^{-1} with the zero contour highlighted by the thick solid contour and in (b) is 2.5 m s^{-1} starting at 2.5 m s^{-1}. Horizontal lines bracket the period for which time-averaged quantities are obtained.

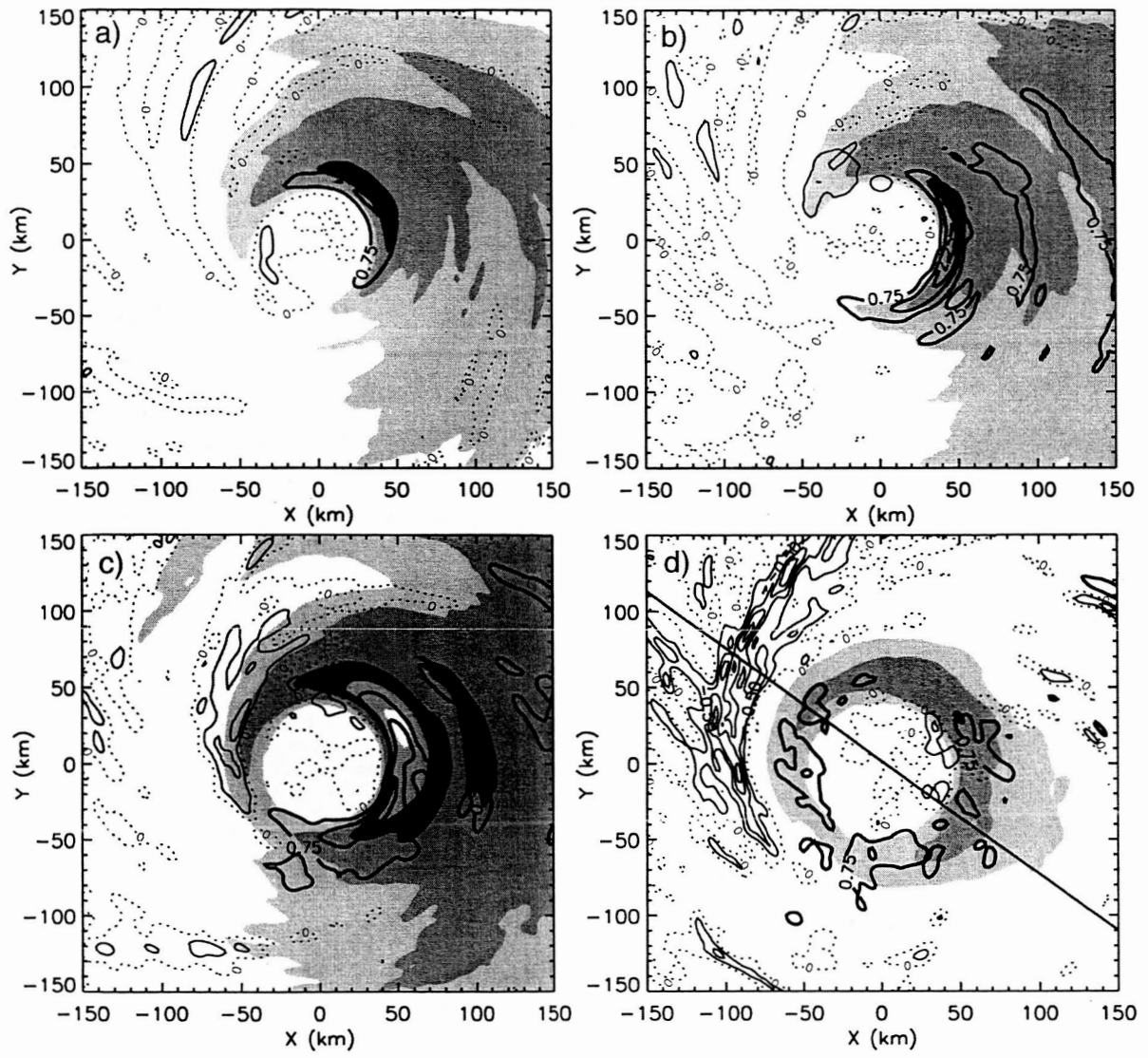

Figure 10. Time-averaged total precipitation mixing ratio (shading; sum of rain, snow, and graupel) and vertical velocity (contours). Precipitation contours are at 0.5, 1, 2, 3, and 4 g kg^{-1}. Vertical velocity contours are at intervals of 0.75 m s^{-1} for updrafts (thick solid lines) and 0.25 m s^{-1} for downdrafts (thin solid lines). The zero contour is indicated by dotted lines. Panels show fields at (a) 1.1 km, (b) 5.0 km, (c) 8.2 km, and (d) 12.0 km. The solid line in (d) indicates the location of the vertical cross section in Fig. 11, which extends somewhat beyond the boundaries of the plot in (d).

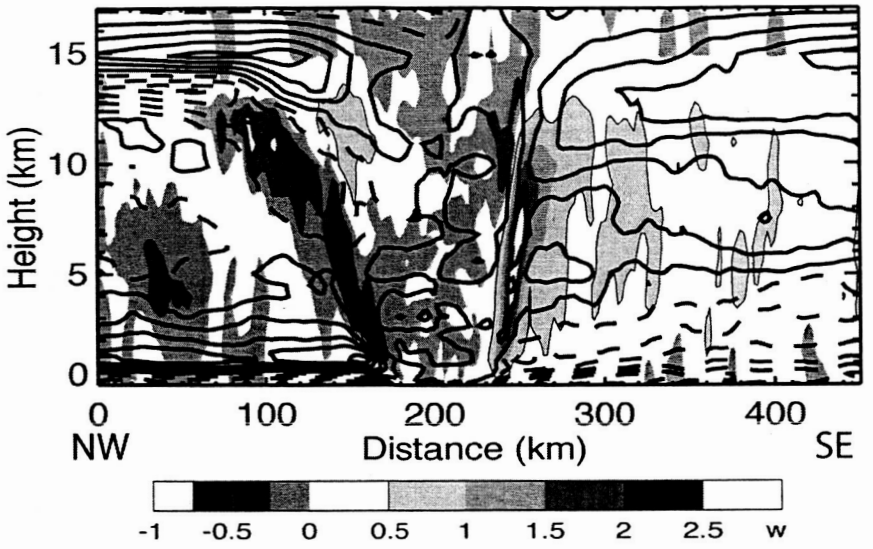

Figure 11. Vertical cross section of time-averaged vertical (shading) and radial velocity (contours) along the line indicated in Fig. 10d. Vertical velocity contours are drawn at 0.25 m s^{-1} for downdrafts and 0.5 m s^{-1} for updrafts. The thin solid contour indicates upward motions greater than 0.5 m s^{-1}. Radial velocities are relative to the time-averaged center location at each height and are drawn at 3 m s^{-1} intervals with positive (negative) values are indicated by solid (dashed) lines.

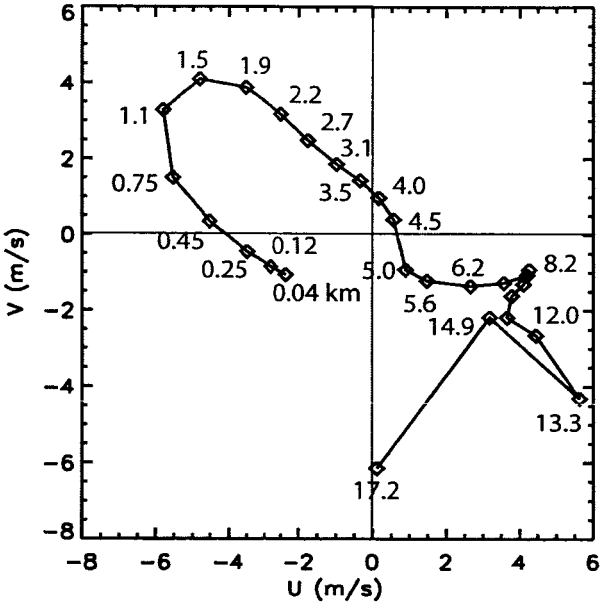

Figure 12. Hodograph of the storm-relative flow from the 6-km grid averaged over a circle of radius 300 km. Diamonds and numbers indicate the heights of the model levels in kilometers.

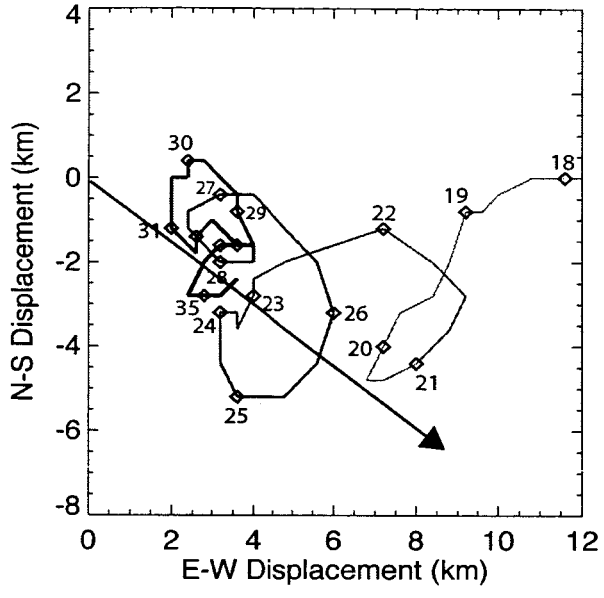

Figure 13. Displacement of the storm center at 8.2 km from the surface center. Time is indicated by the numbers while the line gets thicker and darker with time. The arrow indicates the direction of the shear vector for the layer between 1.1-12 km MSL.

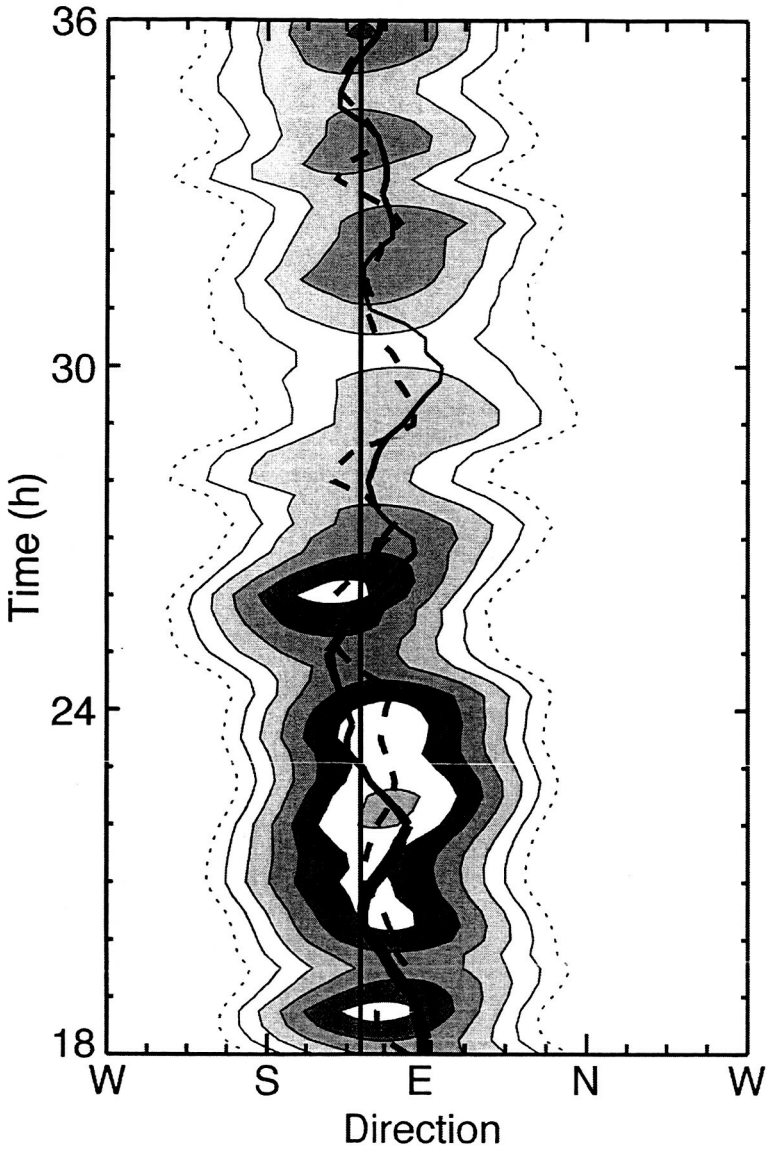

Figure 14. Time-azimuth distribution of wavenumber 1 vertical motion showing updraft contours at an interval of 0.25 m s^{-1} with the zero contour indicated by the dotted line. The dashed line shows the axis of peak wavenumber 1 upward motion. The solid line shows the direction of vortex tilt, with the thickness of the line proportional to vortex tilt (thicker for larger tilt). The solid vertical line indicates the direction of the shear vector.

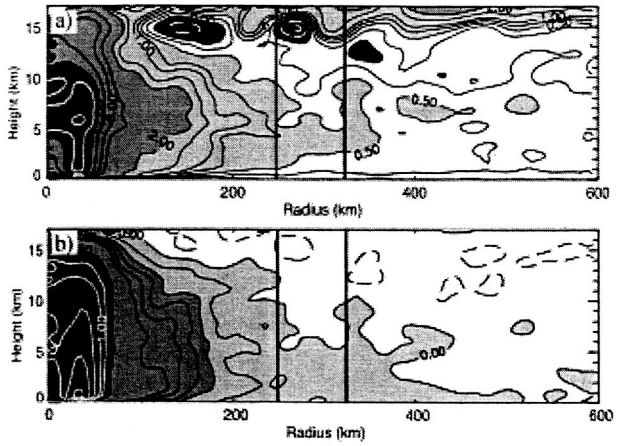

Figure 15. Vertical cross sections of the time-averaged (24-25 h) potential vorticity in (a) and relative vorticity in (b). Contours for PV are drawn at –1, –0.5, 0, 0.25, 0.5, 0.75, 1, 1.5, 2, 4, 6, 9, 12, 15 and 20 PV units (10^{-6} m^2 s^{-1} K kg^{-1}). Negative values are indicated by black shading, positive values by increasingly darker gray shades at 0.5, 2, and 12 PV units. Contours of relative vorticity are at –0.1, –0.05, 0, 0.05, 0.1, 0.15, 0.2, 0.25, 0.5, 0.75, 1, 1.5, 2, and 2.5×10^{-3} s^{-1}. Negative values are indicated by white, positive values by increasingly darker gray shades at 0, 0.1, and 0.5×10^{-3} s^{-1}. Solid straight lines indicate the range of estimated radii where value of the precession frequency equals the density-weighted, vertically integrated angular velocity.

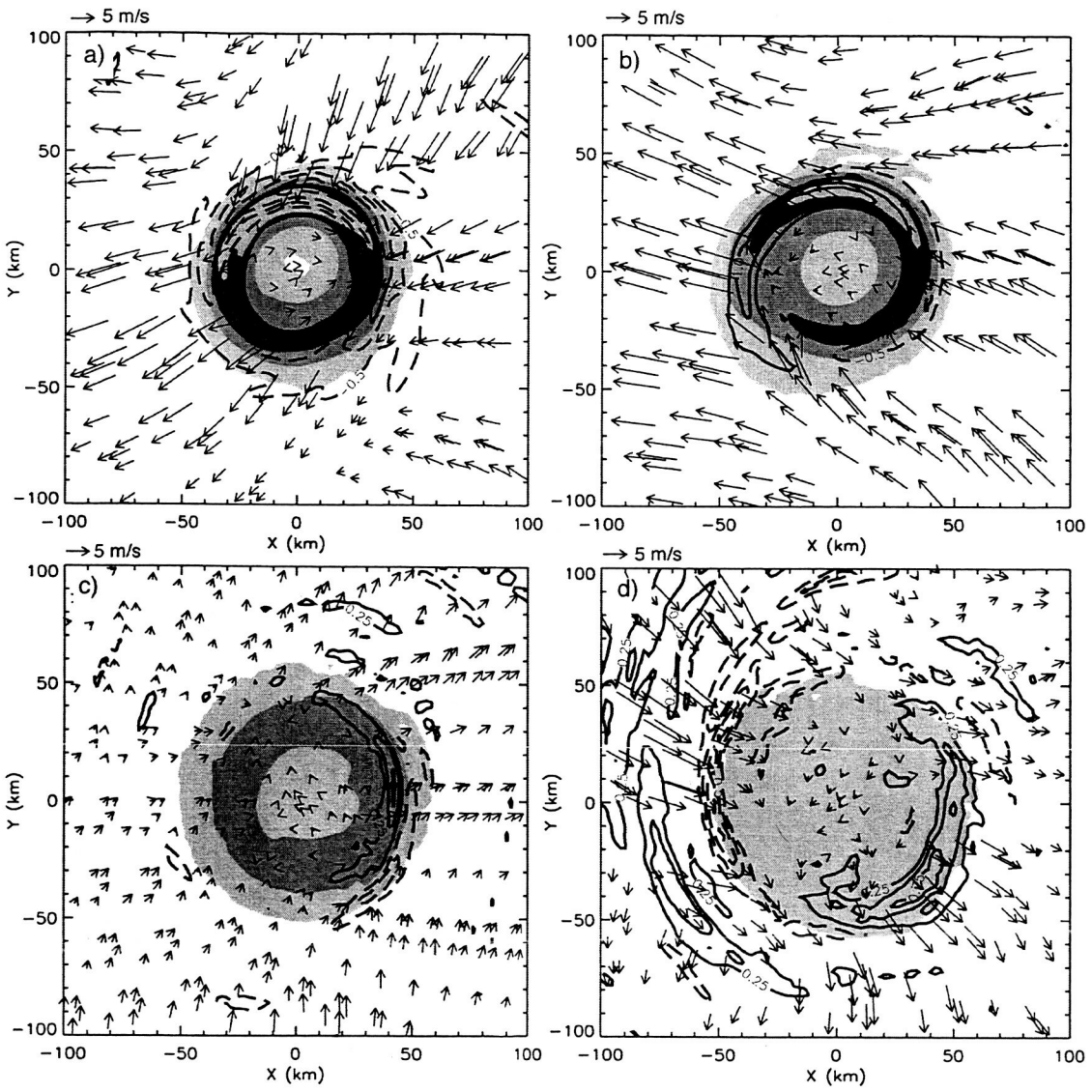

Figure 16. Absolute vertical vorticity (shading), divergence (contours), and asymmetric winds (vectors). Vorticity contours are at 1, 2, 3, and 4×10^{-3} s^{-1}. Divergence contours are at 0.5×10^{-3} s^{-1} intervals, with the zero contour omitted. Positive (negative) values are indicated by solid (dashed) lines. The asymmetric winds are relative to the time-averaged center position at each height. The vector scale is indicated above the upper-left corner. Panels show fields at (a) 0.25 km, (b) 1.1 km, (c) 5.0 km, and (d) 9.9 km.

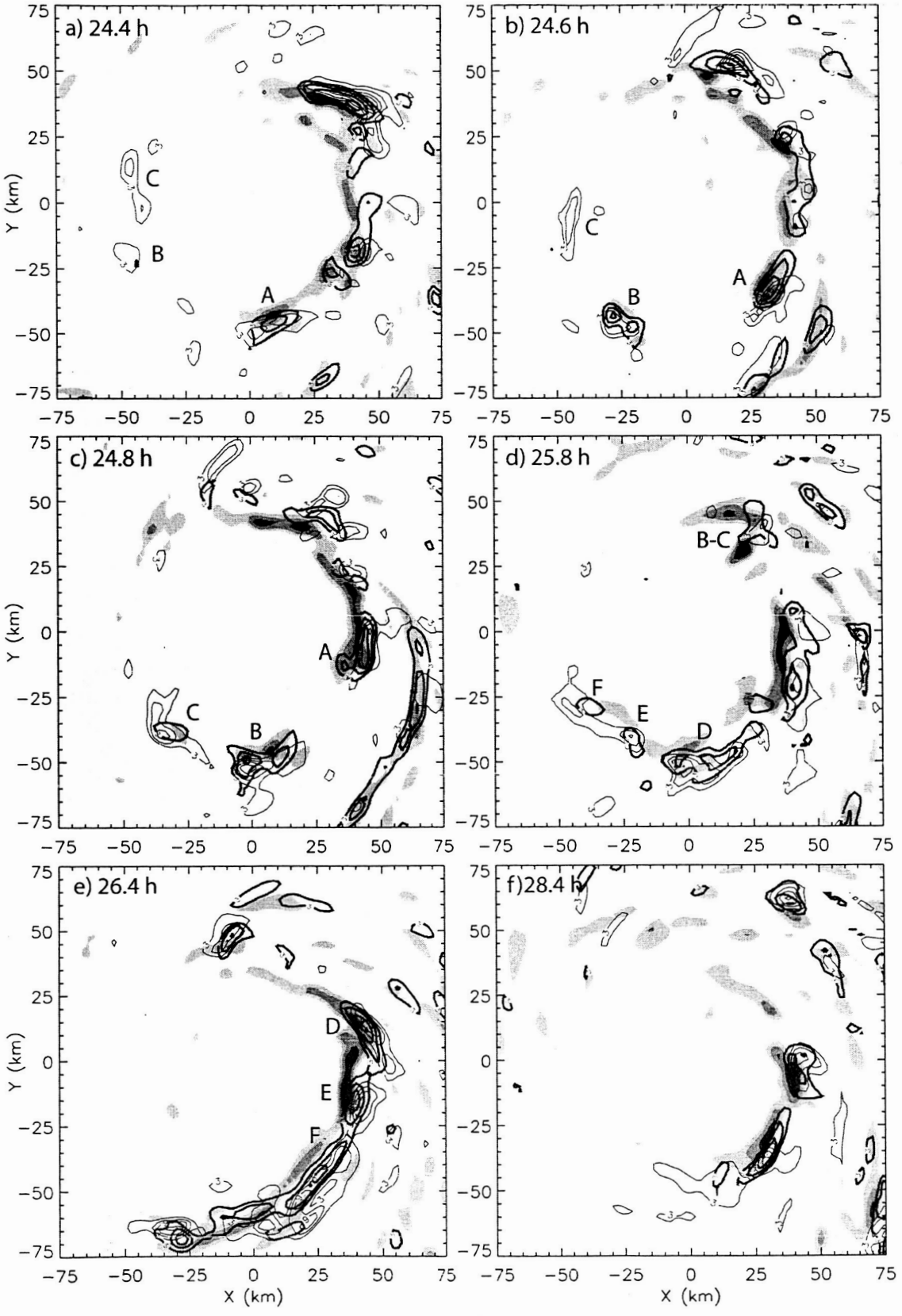
a) 24.4 h
b) 24.6 h
c) 24.8 h
d) 25.8 h
e) 26.4 h
f)28.4 h
A
B
C
B-C
D
E
F
Y (km)
X (km)
75
50
25
0
−25
−50
−75

Figure 17. Vertical velocity at 1.9, 5.0 , and 8.2 km. Shading shows updrafts at 1.9 km MSL at contour levels of 1.5, 3, 4.5, and 6 m s^{-1}. Thick gray contours show updrafts at 5.0 km while thin dark contours show updrafts at 8.2 km at values of 3, 6, 9, and 12 m s^{-1}. The time corresponding to each panel is shown in the upper-left corner. Letters indicate updrafts discussed in the text.

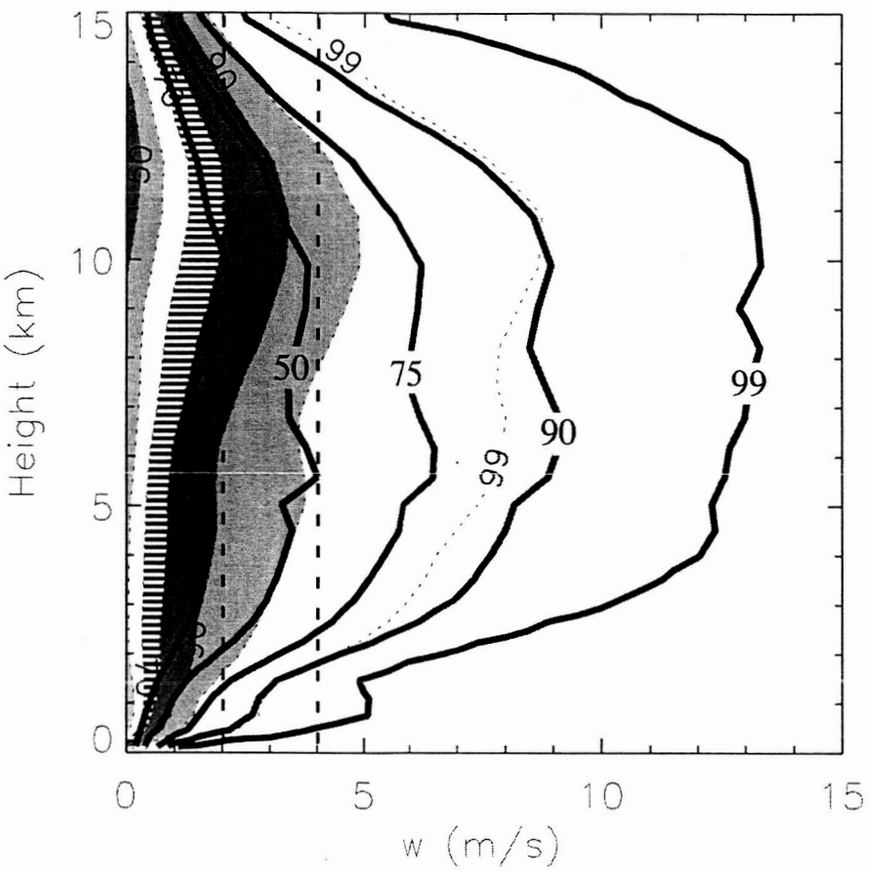

Figure 18. Shading indicates the cumulative frequency of the percentage of the eyewall area occupied by updrafts less than the indicated value. Contours are drawn at 10% intervals, with additional contours at 95 and 99%. Thick lines show the cumulative frequency of total eyewall condensation occurring in updrafts less than the indicated values.

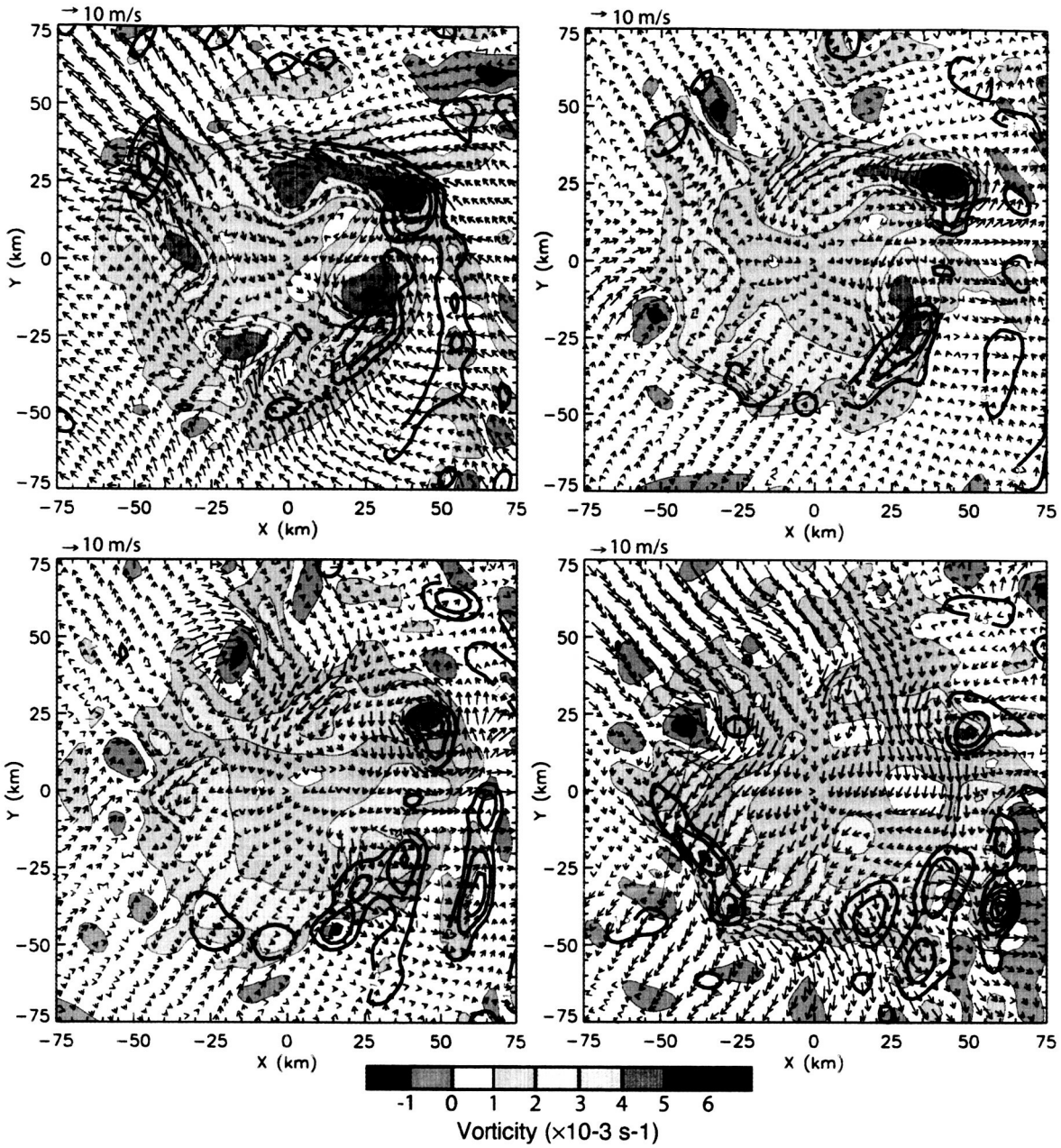

Figure 19. Absolute vorticity (shading), vertical velocity (contours, updrafts only), and storm-relative asymmetric wind vectors at 25.6 h at (a) 1.1 km, (b) 3.1 km, (c) 5.0 km, and (d) 8.2 km MSL. Contour interval for vorticity is 1×10^{-3} s^{-1}. Contours of vertical motion are at 1.5 m s^{-1} intervals starting at 1.5 m s^{-1}. Asymmetric wind vectors are obtained by subtracting the azimuthally averaged radial and tangential winds. The vector scale is indicated above the upper-left corner of each panel.

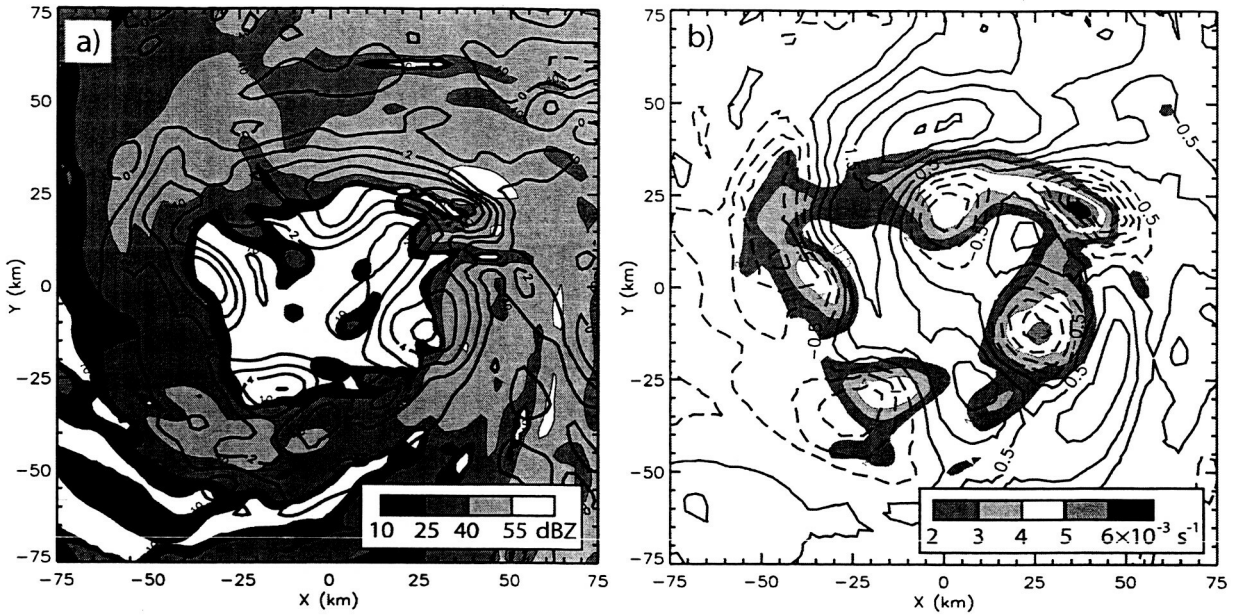

Figure 20. (a) Simulated radar reflectivity (shading) and absolute vorticity at 25.6 h and 1 km MSL. Contour interval for vorticity is 1×10^{-3} s^{-1}. (b) Absolute vorticity (shading) and pressure perturbation (contours). Pressure perturbation is obtained by subtracting the azimuthal mean pressure. Contour interval is 0.5 hPa. In (a) and (b), positive (negative) values are indicated by solid (dashed) lines.

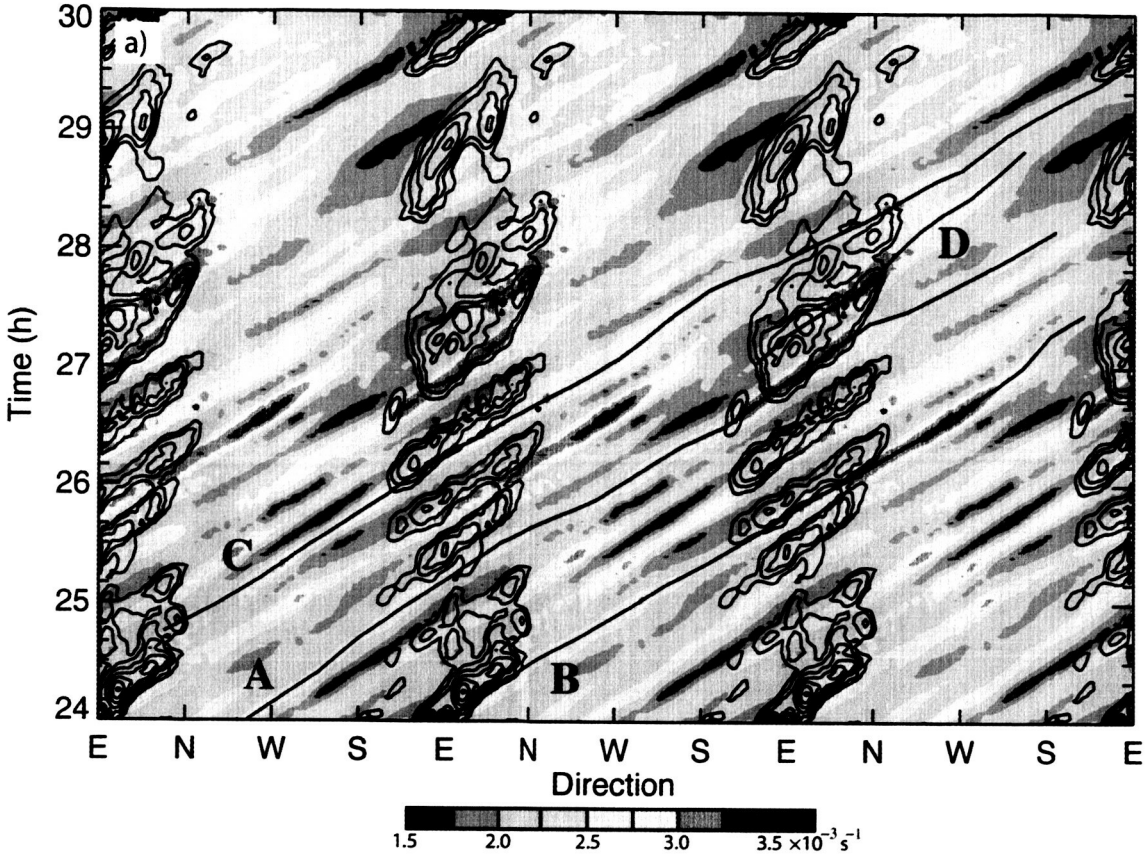
a)
30
29
28
27
26
25
24
Time (h)
A
B
C
D
E N W S E N W S E N W S E
Direction
1.5 2.0 2.5 3.0 3.5 ×10⁻³ s⁻¹

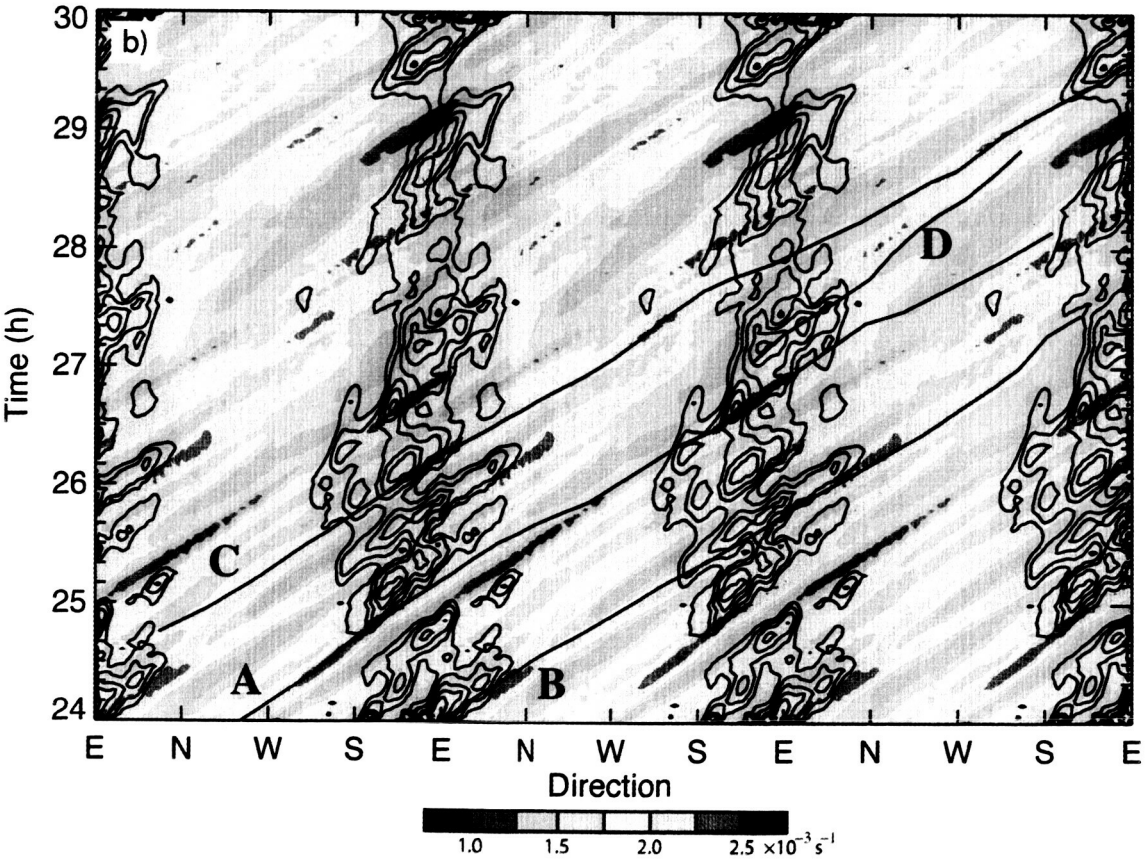
b)
30
29
28
27
26
25
24
Time (h)
A
B
C
D
E N W S E N W S E N W S E
Direction
1.0 1.5 2.0 2.5 ×10⁻³ s⁻¹

Figure 21. Time-azimuth distributions of radially averaged (20-54 km) absolute vorticity (shading, contour interval of 0.25×10^{-3} s^{-1} starting at 1.25×10^{-3} s^{-1}) and vertical velocity (contours, 0.1 m s^{-1} intervals starting at 0.6 m s^{-1}) at (a) 1.1 km and (b) 3.1 km. The plot has been extended to three revolutions around the center. Solid lines follow individual vorticity disturbances, or mesovortices, at 1.1 km and are also overlaid on the 3.1 km fields for comparison. Letters label features described in the text and are unrelated to similar labeling in Fig. 17.